

# Detecting Skyrmions using Implanted Muons



Jordan Mark Wiseman

Supervisor: Professor Tom Lancaster

Thesis presented for the degree of Master of Physics (MPhys)  
Durham University, Department of Physics

April 2021

## Abstract

Muon spectroscopy techniques ( $\mu$ SR) are being increasingly applied in experiments to determine the magnetic field distributions within ever more complex magnetic crystal structures (such as molecular magnets). Such crystal structures are composed of units cells of potentially hundreds of atoms and hence exhibit a host of crystallographically inequivalent muon stopping sites. Hence the principle limitation that the  $\mu$ SR technique faces is interpreting measured polarization curves to deliver detailed information about the local magnetic field environments experienced by embedded muons across the array of stopping sites. A solution is presented in the form of computer simulations (encoded in Python) that predict the internal field distributions in a sample crystal structure for a unique muon stopping site. The model is used to study the swirling, particle-like pattern of spins known as a magnetic skyrmion. Magnetic skyrmions are of particular interest due to their proposed usage as novel information elements in spintronic devices. The model is used to simulate the field distributions within hexagonal magnetic skyrmion lattices. With the local field distribution calculated as a result of magnetic dipole and applied field contributions. Resulting field distributions are shown to be dictated by the underlying skyrmion spin texture. It is also shown that increased dipole field cancellation occurs for skyrmions separated by larger distances. Resulting in distributions of smaller variance. Comparison to experimental determined distributions verifies these findings and shows the strength of the simplistic model. Resulting polarization curves are plotted for each distribution, in order to demonstrate the ability of the technique in predicting the expected asymmetry spectra of  $\mu$ SR experiments.

# Contents

<b>1</b>	<b>Introduction</b>	3
<b>2</b>	<b>Theory</b>	4
2.1	Skyrmions in chiral magnets	4
2.2	Muon spin rotation ( $\mu$ SR) experiments	6
<b>3</b>	<b>Numerical model development</b>	9
3.1	Spin structure generation	9
3.2	Local magnetic field strength calculation	10
3.3	Convergence tests	11
3.4	Lattice modelling method and distribution calculations	12
<b>4</b>	<b>Results and discussion of field simulations</b>	14
4.1	Probability distributions for FM and AFM structures	14
4.2	Probability distributions for helical and conical structures	15
4.3	Skyrmion lattice structures	17
4.4	Stable skyrmion lattice field distributions	18
4.5	Meta-skyrmion lattice field distributions	21
4.6	Statistical analysis of $p(B)$ distributions	23
4.7	Calculated polarization signals	25
<b>5</b>	<b>Method evaluation</b>	27
<b>6</b>	<b>Conclusions</b>	28
<b>7</b>	<b>Acknowledgements</b>	28
<b>References</b>		28
<b>Appendix A Error Appendix</b>		31
<b>Appendix B. Additional Polarization Curves</b>		33
<b>Appendix C. Python code: <math>p(B)</math> modelling code</b>		35

## 1 Introduction

Muons were first proposed as possible probes of magnetic structures in 1957 by Richard Garwin. Who suggested that polarized muons could be used for exploring the microscopic field distributions produced by magnetic systems [1]. Since that time the technique has progressed to laboratory generated, spin polarized muons being injected into a wide variety of samples. The positive muon ( $\mu^+$ ) has a small mass (1/9<sup>th</sup> the mass of a proton) and possesses a large magnetic moment resulting in the muon being highly susceptible to perturbation by weak magnetic fields. Making the muon a perfect candidate as a probe of microscopic magnetic field distributions [2]. Injected muons stop at interstitial positions (space between atoms) within crystals known as stopping sites and subsequently decay in a three body process that generates positrons. During this decay positrons are ejected along the muon spin axis. Owing to interactions between the muon and the local magnetic field environment, the spatial distribution of emitted positrons may be used to glean information about the interior field distribution of a sample. This mechanism constitutes the fundamental principle of the  $\mu$ SR spectroscopy technique and will form the basis of investigations discussed in this report [3, 4].

One such magnetic system studied using  $\mu$ SR techniques is the magnetic skyrmion. As seen in figure 1(a), a skyrmion is a swirling, localised pattern of Heisenberg spins supported on an atomic lattice. With a central spin aligned antiparallel to spins surrounding the skyrmion (outside of the skyrmion radius). Moving radially outward from the centre of the skyrmion, the spin orientation rotates in a helix (as shown in figure 1(b)) [5]. It is this area of research that this report will concern itself. The existence of skyrmions was first proposed by the physicist Tony Skyrme, who theorised that skyrmions were analogous to nucleons of matter. Whilst their initial introduction as fundamental particles was disproved, it has been suggested that skyrmions may be excitations of materials such as quantum Hall fluids and superconductors [5, 6]. The earliest reported sightings of skyrmions was at Bell Labs in the United States, when "magnetic bubbles" were identified in thin film ferromagnets [7]. The theory followed these discoveries and following the development of the Ginz-Landau (GL) theory for chiral magnets, a vortex like solution was postulated by Bogdanov and Yablonskii in 1989 [8]. This signified the establishment of modern skyrmion theory with the first prediction of the skyrmion lattice [7]. The technique for studying skyrmions discussed in this report represents a simple model of skyrmion evolution across a range of host crystals as a result of changing external conditions.

Continued interest in understanding the processes powering skyrmion dynamics is being generated by their potential application within future novel spintronic devices such as information storage or logic devices. The high stability of skyrmion structures, as well as their small size and ease of manipulation using an electrical current, makes them ideal candidates as the operating bits within spintronic devices [9]. Switching between ferromagnetic and skyrmionic states describes a possible bit operation system within information storage systems. Devices recognise this change in spin arrangement through detection of the topological charge associated with a skyrmion structure. With magnetisation at the centre of the skyrmion having opposite polarity to the surrounding structure [10, 11]. Solid state systems using skyrmion operating bits would also require significantly smaller current densities to manipulate their structures, leading

to more energy efficient and environmentally friendly devices [12].

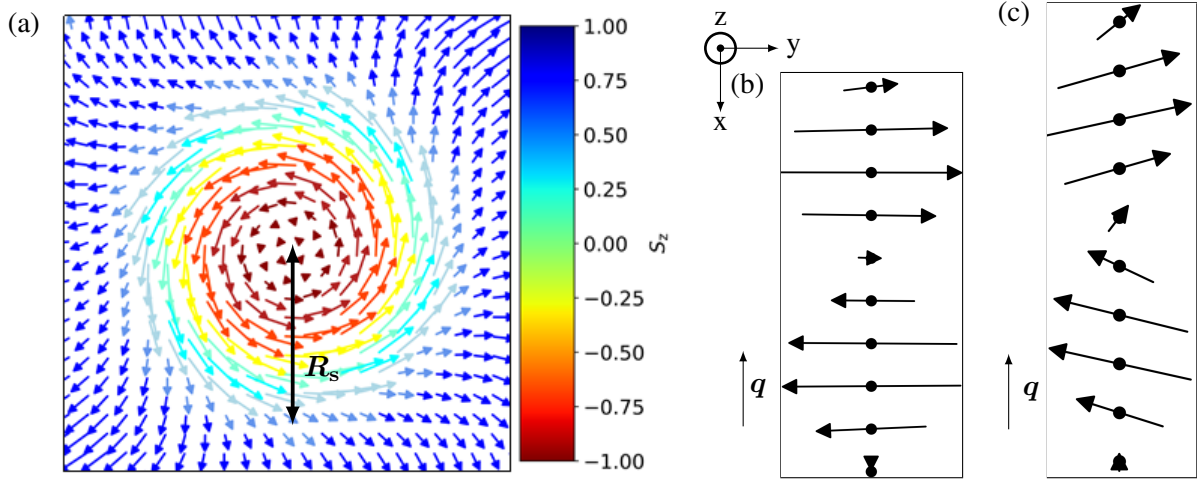


**Figure 1:** (a) An individual skyrmion viewed from above with arrows representing individual Heisenberg spins of  $S = (S_x, S_y, S_z)$ . The surrounding spin texture (blue) is ferromagnetic in nature, with spins of  $S \parallel (0,0,1)$ . The rotation of individual spins is indicated via the colour gradient of  $S_z$ . The skyrmion radius is indicated at  $R_s$  (b) Bloch wall, helical spin structure. With a corresponding modulation vector  $\mathbf{q}$ . (c) Conical spin structure also using  $\mathbf{q}$  [13].

This report will describe the development of a computational method capable of calculating the probability distribution,  $p(B)$ , of internal magnetic fields within a sample. The method will be demonstrated using a skyrmion lattice. The expected muon spin polarization curves for transverse field (TF) geometry  $\mu$ SR experiments studying magnetic skyrmions, will be produced and compared to experimental results. Distributions will first be modelled for ferromagnetic (FM) and antiferromagnetic (AFM) structures, as well as helical and conical spin structures (figures 1(b) and (c) respectively). Features present within these distributions will be used to analyse distributions determined for skyrmion lattices. To relate distributions to physical spin structures, the spatial distribution of fields will be presented. Additionally the method outlined in this report provides a solution to the principle limitation faced by  $\mu$ SR experiments; the problem of distinguishing contributions to polarization curves from muons embedded at a large number of possible stopping sites. A magnetic system generating an inhomogeneous internal field distribution, means each stopping site within a unit cell experiences a different local field strength [14]. The resulting muon polarization function will therefore depend on contributions the field distribution and which sites muons embed at [2, 14]. This paper describes one of the few examples of a direct determination of  $p(B)$  experienced by a single stopping site within a unit cell.

## 2 Theory

### 2.1 Skyrmions in chiral magnets

The magnetic skyrmion is a topological defect of the ferromagnetic spin state possessing particle-like properties. The specific skyrmion spin configuration observed in figure 1 is classed

as a Bloch skyrmion. Taking diametric cuts across a Bloch skyrmion reveals the helical spin structure known as a Bloch domain wall, as seen in figure 1(b). The Bloch wall is characterised by spins rotating in a plane perpendicular to the propagation direction of the helix [7]. Skyrmion structures are categorized using a quantity known as the winding number,  $w$ , describing the number of full spin rotations ( $2\pi$ ) occurring across the width of a skyrmion. The winding number is expressed as

$$w = \frac{1}{4\pi} \int dx^1 dx^2 \hat{\phi} \cdot \left( \frac{\partial \hat{\phi}}{\partial x^1} \times \frac{\partial \hat{\phi}}{\partial x^2} \right), \quad (1)$$

where  $\hat{\phi}$  is the normalised local magnetic field and is calculated using  $\hat{\phi} = \phi/|\phi|$ . Spins are located using the spherical coordinates  $x^1$  and  $x^2$ . Bloch skyrmions possess winding numbers of  $w = 1$ , with a single  $2\pi$  spin rotation across their diameter [5, 15].

Stable skyrmion spin textures arise from competing interactions within a magnetic structure. Below some critical temperature  $T_c$ , magnetic materials undergo a transition to the ferromagnetic phase, where spins ( $\mathbf{S}$ ) align parallel to each other. This alignment is caused by the Heisenberg exchange interaction, which occurs between neighbouring spins. A GL description of this interaction stipulates a Hamiltonian of the form

$$H_{\text{FM}} = -J \mathbf{S}_1 \cdot \mathbf{S}_2 \quad (2)$$

Where  $J$  is a ferromagnetic exchange constant and  $\mathbf{S}_1$  and  $\mathbf{S}_2$  are nearest neighbour spins [7]. This interaction seeks to minimise the overall energy of the system via parallel spin alignment. One modelling assumption is that the above equation is invariant across the lattice [7, 16].

The magnetic materials hosting the skyrmions are non-centrosymmetric crystal structures exhibiting broken inversion symmetry. It is such materials that are discussed in this report. Broken symmetry stimulates competition between the ferromagnetic exchange coupling and an anisotropic interaction originating from relativistic spin orbit coupling. This yields the non-collinear Dzyaloshinskii–Moriya (DM) interaction [17]. The DM interaction adds a second term to the non-centrosymmetric crystal Hamiltonian:

$$H_{\text{DM}} = \mathbf{D} \cdot (\mathbf{S}_1 \times \mathbf{S}_2), \quad (3)$$

where  $\mathbf{S}_1$  and  $\mathbf{S}_2$  denote nearest neighbour spins. The coupling vector,  $\mathbf{D}$ , is dependent on the arrangement of neighbouring spins within the crystal structure. Any symmetry operation capable of transforming  $\mathbf{S}_1 \leftrightarrow -\mathbf{S}_2$  implies a center of inversion exists between the two spins and so  $H_{\text{DM}} = -H_{\text{DM}}$ . Therefore  $H_{\text{DM}}$  and  $\mathbf{D} = 0$ . Hence this energy contribution is only found within crystals displaying no center of symmetry, such as chiral magnets [18]. Whilst the Heisenberg interaction dictates the interactions between neighbouring spins, it is the DM interaction that is responsible for generating the non-collinear spin textures found in helical, conical and Bloch skyrmions [17]. A spiral spin structure minimises this free energy description and hence a helical structure is the expected ground state for a positive DM energy  $D > 0$  [7].

The final contribution to the free energy is required to stabilise skyrmions of a defined radius.

The swirling pattern of spins due to the DM interaction comes with an associated energy term, which is expressed as

$$F_{\text{DM}} = D \int d^d x \mathbf{S} \cdot (\nabla_d \times \mathbf{S}) \propto \mathbf{R}_s. \quad (4)$$

Where  $d$  is the dimensionality of the system. Revealing the DM interaction to scale linearly with  $\mathbf{R}_s$ . Meaning with no other energy contributions a spin structure extending over the entire spin lattice is expected (if the integral is negative). Derrick's theorem tells us that a skyrmion can only form at the instance where the free energy reaches a saddle point with increasing  $\mathbf{R}_s$ . As no stationary point exists for just a DM term scaling linearly with  $\mathbf{R}_s$ , a skyrmion cannot exist with just the DM and Heisenberg exchange interactions. It is at this point that a third energy contribution is introduced via the application of an externally applied field ( $\mathbf{B}_{\text{ext}}$ ). This energy contribution is known as the Zeeman term and has a quadratic dependence on  $\mathbf{R}_s$ :

$$F_Z = - \int d^d x \mathbf{B}_{\text{ext}} \cdot \mathbf{S} \propto \mathbf{R}_s^2. \quad (5)$$

The result of this integral is a positive contribution to the energy. The final energy of the system is now given  $E_s = E_0 - c_{DM} R_s + c_Z R_s^2$ , where  $c_{DM}$  and  $c_Z$  are constants. This system yields a stationary energy value for  $R_s > 0$ . Therefore satisfying Derrick's theorem for a stable spin texture of finite size. The spin configuration minimising the energy of the crystal is the skyrmion lattice (SKL) phase. Which may be considered a superposition of several spiral spin waves [5, 17]. The 2D SKL is a triangular arrangement of skyrmions which, when extended to 3 dimensions, results in a structure of tubes analogous to the vortex lattice observed in type II superconductors [15, 18, 19].

The full Hamiltonian describing this crystal system is given as:

$$H = \sum_{ij} -JS_i \cdot S_j + D_{ij} \cdot (S_i \times S_j) - \sum_i g\mu_B \mathbf{B}_{\text{ext}} \cdot \mathbf{S}_i, \quad (6)$$

where  $g$  is the Landé g-factor and  $\mu_B$  is the Bohr magneton constant which is equal to  $9.3 \times 10^{-24} \text{ JT}^{-1}$ . All other terms are as previously defined. Competition between the described energy terms results in a complex magnetic field strength vs temperature phase diagram. The SKL phase arises at applied field strengths causing a transition between the helical (figure 1(b)) and conical (figure 1(c)) spin textures and below a critical temperature  $T_c$ . Additionally, thermal fluctuations ensure that the skyrmion lattice is the equilibrium phase of a sample just below  $T_c$ . This small region of the phase diagram in which a stable skyrmion exists is known as the A-phase [17–19].

## 2.2 Muon spin rotation ( $\mu$ SR) experiments

Muon spectroscopy has become a powerful experimental tool since its development in the 1970s. The technique provides the ability to penetrate into a material to examine internal magnetic field distributions. In performing a  $\mu$ SR experiment positive muons with spins polarized antiparallel to their momentum are implanted into the bulk of a material. Implanted muons sub-

sequently stop at random interstitial positions within the sample (stopping sites) and then decay after a time  $t$  [4]. The geometry for transverse field experiments is shown in figure 2(a). It is assumed the stopping interactions are Coulombic in nature and therefore do not affect the spin orientation [2]. The muon decay produces positron particles in a process that fails to conserve parity, meaning emitted positrons are aligned parallel to the muon's spin direction at the time of decay [20].

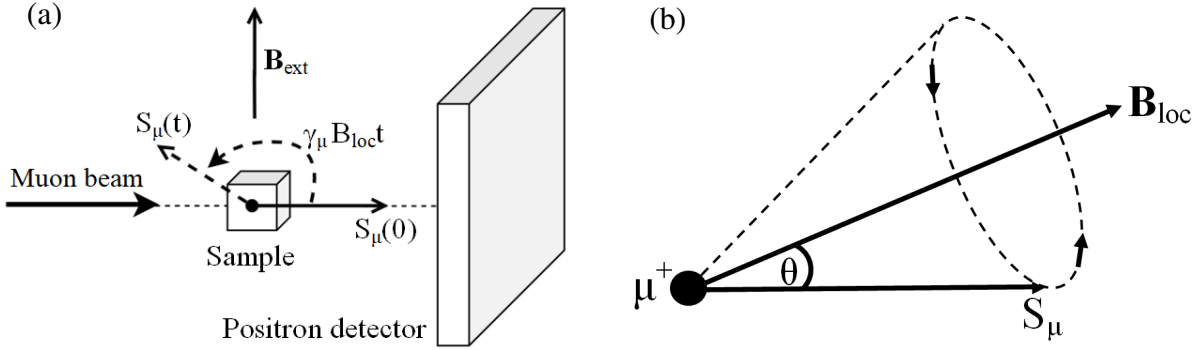


**Figure 2:** (a) Geometry of the transverse field (TF)  $\mu$ SR experiment. The externally applied field  $B_{\text{ext}}$  is orthogonal to the momentum of embedded muons. A second detector placed behind the muon beam trajectory has been omitted to clarify the muon beam trajectory. The Larmour precession of muon spin  $S_\mu$  due to a local magnetic field  $B_{\text{loc}}$  is indicated via  $\gamma_\mu B_{\text{loc}}t$ . Positrons are emitted along the axis of  $S_\mu(t)$  [2,4]. (b) Precession of muon ( $\mu^+$ ) spin ( $S_\mu$ ) in a local magnetic field direction  $B_{\text{loc}}$ . Demonstrating the rotation of the muon spin direction around a cone of semi angle  $\theta$  [3].

During an interaction with a local magnetic field  $B_{\text{loc}}$ , the muon-spin undergoes Larmor precession (figure 2(b)), where the spin orientation precesses around  $B_{\text{loc}}$  with an angular frequency of  $\omega_\mu = \gamma_\mu B_{\text{loc}}$  [3]. Where  $\gamma_\mu$  is an experimentally measured constant known as the gyromagnetic ratio and has a value of  $2\pi \times 135.5 \text{ MHz T}^{-1}$  [14]. The classical interpretation of the generation of this rotation relies on the local magnetic field creating a torque on the magnetic moment of the muon. The torque ( $\tau$ ) may be expressed as a rate of change of muon spin  $S_\mu$ ,

$$\tau = \boldsymbol{\mu} \times \mathbf{B}_{\text{loc}} = \frac{d\mathbf{S}_\mu}{dt}, \quad (7)$$

where  $\boldsymbol{\mu}$  is the magnetic moment of the muon [4]. This precession results in emitted positron distributions that can be directly related to the local magnetic field environment surrounding an implanted muon. Which in turn may be interpreted to gain an understanding of the local spin textures generating such fields. The number of positrons measured at detectors located either side of the sample, is described using the normalised asymmetry function, given by

$$A(t) = \frac{N_B(t) - N_F(t)}{N_B(t) + N_F(t)}. \quad (8)$$

Where  $N_B$  and  $N_F$  are the number of positrons detected behind and in front of the sample space respectively [3]. This asymmetry term is related to the polarization of the muon via

$$A(t) = aP_\alpha(t), \quad (9)$$

where  $a$  is the initial symmetry (at  $t = 0$ ) and depends on the experimental geometry. For most experiments  $a \approx 0.25$  [3, 4]. The muon polarization function  $P_\alpha(t)$ , which describes the evolution of the polarization of a muon along some Cartesian axis  $\alpha$  over time, is expressed as

$$P_\alpha(t) = \cos^2 \theta + \sin^2 \theta \cos(\gamma_\mu B_{\text{loc}} t), \quad (10)$$

where  $\theta$  is the angle between  $\mathbf{B}_{\text{ext}}$  and the initial muon-spin direction  $\mathbf{S}_\mu(0)$ . This result is derived using the Larmour equation. From the geometry of a TF experiment set-up  $\theta = \pi/2$  and hence only the second term of equation 10 is used [4].

For the simulations considered within this paper the muon ensemble (large number of embedded muons) does not experience a constant  $\mathbf{B}_{\text{loc}}$  at individual stopping sites and therefore a distribution of fields must be considered. The field distribution causes a dephasing of the muon spins within the ensemble. If the applied field is large enough relative to the internal field distribution such that  $\mathbf{B}_{\text{ext}} \geq 5\Delta/\gamma_\mu$  then the muon polarization function only probes the field distribution along the axis of  $\mathbf{B}_{\text{ext}}$ . Where  $\Delta^2/\gamma_\mu^2$  is equal to the variance (second moment) of the distribution  $p(B)$ . For the TF experimental geometry this means  $\alpha$  is set along the x-axis [2]. The time evolution of the muon-spin polarization function  $P_x(t)$  can be expressed as a cosine Fourier transform over all possible field values

$$P_x(t) = \int_{-\infty}^{\infty} dB p(B) \cos(\gamma_\mu B_{\text{loc}} t), \quad (11)$$

where  $p(B)$  is the distribution of static local magnetic field strengths and all other terms are as previously defined. Through a determination of  $p(B)$  the spin polarization evolution can be plotted and used for comparison with experimental results [2, 20].

Due to the large number of muons embedded into a sample during an experiment only the average muon spin  $\langle \mathbf{S}_\mu \rangle$  needs to be considered. Hence the polarization function may be rewritten to encompass this information as

$$\mathbf{P}_x(t) = \frac{\langle \mathbf{S}_\mu(t) \rangle}{\mathbf{S}_\mu(0)}, \quad (12)$$

where  $\mathbf{S}_\mu(0)$  is the initial muon spin polarization [2, 4]. The relaxation rate of a polarization function describes the envelope encapsulating oscillations of the polarization function and may be described as

$$\Delta^2 = \gamma_\mu^2 \langle \Delta B_\alpha^2 \rangle \quad (13)$$

Where  $\langle \Delta B_\alpha^2 \rangle$  is the variance of  $p(B)$  and all other terms are as previously stated. This will prove a useful term for discussing calculated forms of  $P_x(t)$  [2, 20]. Physical experiments typically work through the above equations in the described order, using collected positron numbers to determine  $p(B)$  of a target sample. This report focuses on a direct determination of  $p(B)$  for skyrmion lattices, which is then used to predict  $P_x(t)$ .

### 3 Numerical model development

Within this section the model method framework is presented. Describing the steps encoded within a Python program (appendix C) to determine  $P_x(t)$  from  $p(B)$ . First the generation of helical and skyrmion spin structures will be discussed. The numerical methods for calculating the magnetic field strength at a single location within a lattice is then discussed. Following this, the results of convergence tests are reviewed to guide the choice of lattice size parameters. Finally a description of how a field distribution is generated and  $P_x(t)$  calculated is presented.

#### 3.1 Spin structure generation

In order to calculate the spin configuration,  $\mathbf{S}(\mathbf{r})$ , for a position  $\mathbf{r}$  within a sample lattice due to the presence of a helical spin structure, the following relationship is used  $\mathbf{S}(\mathbf{r}) = \mathbf{S}_h(\mathbf{r})/|\mathbf{S}_h(\mathbf{r})|$  where

$$\mathbf{S}_h(\mathbf{r}) = (S_\alpha e^{i\mathbf{q}\cdot\mathbf{r}} + S_\alpha^* e^{-i\mathbf{q}\cdot\mathbf{r}}). \quad (14)$$

The complex vector  $\mathbf{S}_\alpha$  is composed of vector elements  $\mathbf{a}_\alpha + i\mathbf{b}_\alpha$ , describing the plane in which the spin components rotate [18]. Each modulation vector  $\mathbf{q}$  describes the propagation direction of one spin helix using equation (14) and is expressed as

$$\mathbf{q} = \frac{2\pi}{\lambda_{\text{skl}}} \hat{\mathbf{q}}, \quad (15)$$

where  $\lambda_{\text{skl}}$  is the skyrmion wavelength ( $\lambda$  for non-skyrmion structures) [22]. Spins within a helix rotate perpendicular to  $\hat{\mathbf{q}}$ . The skyrmion wavelength is responsible for the arrangement of individual skyrmion within a lattice. This can be related to the interactions dictating the spin structure via

$$|\mathbf{q}| = \kappa = \frac{D}{J} \quad (16)$$

the ratio of the DM energy  $D$  to the ferromagnetic exchange energy  $J$ . For  $D > 0$  a chiral magnet favours helices with right handed chirality [7]. For a ferromagnetic (FM) spin structure  $\mathbf{q}$  has direction  $(0, 0, 0)$  and for an antiferromagnetic (AFM) structure a direction  $(\pi, \pi, \pi)$  is used [14]. The hexagonal skyrmion lattice is produced using three modulation vectors which form an equilateral triangle (multi-q wavevector approach) [5]. Therefore a skyrmion lattice may be considered a superposition of three spiral helices. Using equation (14) and adding a term  $S_0^z$  to represent the induced magnetization directed parallel to any applied fields present ( $\mathbf{B}_{\text{ext}}$ ), yields the final expression required to generate a skyrmion spin texture:

$$\mathbf{S}(\mathbf{r}) = (0, 0, S_0^z) + \sum_{\nu=1}^3 (\hat{e}_z \cos(\mathbf{q}_\nu \cdot \mathbf{r}) + \hat{e}_i \sin(\mathbf{q}_\nu \cdot \mathbf{r})). \quad (17)$$

Where  $\hat{e}_z \parallel (0, 0, 1)$  and  $\hat{e}_i \perp \mathbf{q}$  [20, 24]. To determine  $\hat{e}_i$ , a 3D rotation matrix is used. Where Euler's rotation theorem is used to describe any 3D vector rotation using three rotation angles  $(\theta, \phi, \psi)$ . This matrix rotates an initial vector  $(1, 1, 0)$  about the z-axis through an azimuthal angle  $\phi$ , given as  $\pi$  plus the angle subtended by  $\mathbf{q}$  and the x-axis [25]. The full rotation matrix

is quoted within the code included in appendix C.

Whilst it is the spin texture that is plotted using the above equations, the magnetic moment associated with the atom possessing that spin is used for calculating local magnetic field strengths. Therefore, it is useful to convert spins ( $\mathbf{S}$ ) to moments ( $\mathbf{m}$ ) using the relationship

$$\mathbf{m}(\mathbf{r}) = \gamma \mathbf{S}(\mathbf{r}), \quad (18)$$

where  $\gamma$  is the gyromagnetic ratio, and is calculated using  $\gamma = gq_e/2m_e$ . Where  $q_e$  is the charge of the electron,  $m_e$  is the electron mass and  $g$  is the spin g-factor taken as  $\approx 2$  for the calculations undertaken in this report [26, 27]. This relationship will be used extensively throughout this paper and is used to populate each lattice position with a magnetisation of the form  $M\hat{\mathbf{m}}(\mathbf{r})$ , where  $M$  is the magnitude of the magnetic moment for a particular atom in units of  $\mu_B$  (the Bohr-magneton constant) [28]. This is within the context of a Heisenberg spin model where atoms are assigned with a spin in place of the total angular momentum [26].

For conical structures equation (14) is used with only one modulation vector,  $\mathbf{q}_\alpha$ . An additional vector component  $S_0^\alpha$  is then added  $\parallel \mathbf{q}_\alpha$  to account for the applied field needed to generate such structures.

### 3.2 Local magnetic field strength calculation

The local magnetic field at any position within a crystal lattice may be expressed as a sum of several contributing factors

$$\mathbf{B}_{\text{loc}} = \mathbf{B}_{\text{ext}} + \mathbf{B}_{\text{shape}} + \mathbf{B}_{\text{Lorentz}} + \mathbf{B}_{\text{dip}}. \quad (19)$$

The first term  $\mathbf{B}_{\text{ext}}$  is an externally applied magnetic field. For initial simulations concerning AFM and FM structures, this term is omitted as no external field is required to generate the spontaneous alignment observed within these structures. The second term,  $\mathbf{B}_{\text{shape}}$ , includes the contribution due to sample shape effects through demagnetizing fields generated by externally applied fields. It is of greater significance closer to the sharp edges of a modelled sample and therefore can be removed when considering the bulk of a sample. This term disappears when modelling an AFM structure as the total magnetic moment per unit volume tends to 0. The third term,  $\mathbf{B}_{\text{Lorentz}}$ , includes the effect of the Lorentz sphere and can be removed by modelling samples as spheres. It is excluded from calculations undertaken in this report which may be assumed to lie within a larger spherical sample. The fourth term is equal to the contribution arising from local dipole fields generated by individual magnetic moments within the lattice structure  $\mathbf{B}_{\text{dip}}$  [3, 29].

The vector dipole field  $\mathbf{B}_{\text{dip}}(\mathbf{r})$  experienced by a central position within the lattice  $\mathbf{r}_i = (x_i, y_i, z_i)$ , is described by

$$\mathbf{B}_{\text{dip}}(\mathbf{r}) = \sum_j^n \mathbf{D}_j(\mathbf{r}) \cdot \mathbf{m}_j, \quad (20)$$

where  $\mathbf{m}_j$  is a magnetic moment located at some coordinate within the lattice of  $n$  atoms. The dot product is taken between  $\mathbf{m}_j$  and the dipolar tensor matrix  $\mathbf{D}(\mathbf{r})$ , using the following for a

lattice of spins:

$$D_j^{\alpha\beta}(\mathbf{r}_\mu) = \frac{\mu_0}{4\pi r_j^3} \left( \frac{3\mathbf{r}_j^\alpha \mathbf{r}_j^\beta}{R_i^2} - \delta^{\alpha\beta} \right), \quad (21)$$

where  $\mu_0$  indicates the vacuum permeability constant and  $r$  is equal to  $|\mathbf{r}_{ji}| = |\mathbf{r}_j - \mathbf{r}_i|$ . Where  $\mathbf{r}_j$  is the position vector of the magnetic moment ( $\mathbf{m}_j$ ) generating the dipole field, with respect to an origin defined as the centre of a sample [29]. The variables  $r_j^\alpha$  and  $r_j^\beta$  run over the Cartesian axis and yield a  $3 \times 3$  tensor matrix [14].

### 3.3 Convergence tests

Having established a method for calculating  $\mathbf{B}_{\text{loc}}$  at any position within a lattice, convergence tests were then performed to establish a relation between the size of a sample lattice and the numerical noise present within measurements. This test allows for smaller sample sizes to be chosen for future simulations of  $p(B)$  with accuracies consistent with larger samples but with a fraction of the run time [14].

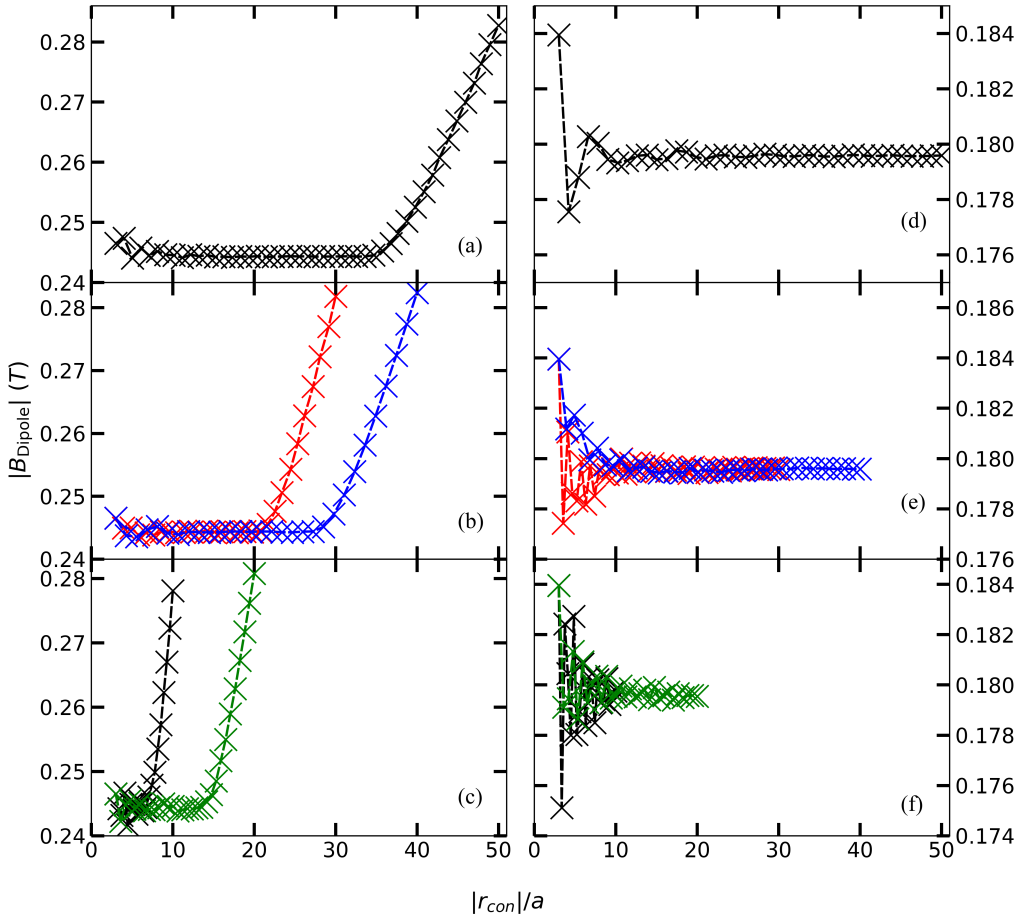


**Figure 3:** Convergence tests performed for increasing lattice sizes of lattice spacing  $a = 4.558 \text{ \AA}$  (a) FM lattice of size  $50a \times 50a \times 50a$  (black). (b) FM lattices of size  $40a \times 40a \times 40a$  (green) and  $30a \times 30a \times 30a$  (red). (c) FM lattices of size  $20a \times 20a \times 20a$  (blue) and  $10a \times 10a \times 10a$  (black). The equivalent convergence tests are seen in panels (d), (e) and (f) for AFM lattices with corresponding colour schemes.

To perform a convergence test a single point ( $\alpha_{\text{test}}$ ) within a sample lattice is chosen at which to measure  $B_{\text{loc}}$ . A sphere of radius  $r_{\text{con}}$ , defined as the convergence radius, is then centered on  $\alpha_{\text{test}}$ . The dipole fields produced by magnetic moments of magnitude  $0.4 \mu_B$  lying within the sphere are included in the summation expressed in equation (20) [32]. The value of  $r_{\text{con}}$  is then increased using increments of one lattice spacing ( $a$ ). The results of convergence tests performed on AFM and FM structures can be seen in figure 3. FM structures are characterized by the parallel alignment of magnetic moments situated on neighbouring lattice positions. The AFM samples are characterized by the antiparallel arrangement of magnetic moments [30]. A lattice spacing of  $a = 4.558 \text{ \AA}$  is used to produce cubic unit cells analogous to the MnSi crystal structure [31]. The measurement position  $\alpha_{\text{test}}$  is set as  $(2.0, 2.0, 3.0) \text{ \AA}$ . This low symmetry location within a unit cell in the bulk of the sample, is chosen to avoid immediate cancellation of all dipole fields.

Considering first the convergence trends produced for a FM structure in panels (a), (b) and (c) in figure 3, it is observed that a constant value of  $B_{\text{loc}}$  is measured within the bulk of the lattice. An increase in lattice size yields a larger region of constant field strengths. The initial consistency in the value of the magnetic field strength is attributed to cancellation between dipole fields of opposite polarity generated by magnetic moments situated on neighbouring planes. As the radius is increased, fields generated close to the surface of a sample are now included (non-bulk magnetic moments). These surface fields experience less cancellation than more central fields and therefore serve to linearly increase the value of  $B_{\text{loc}}$  measured at  $\alpha_{\text{test}}$ . The number of measurements the linear increase occurs over is proportional to the size of the sample lattice.

Now considering the AFM convergence tests seen in panels (d), (e) and (f) in figure 3, a clear convergence to a constant value is seen. For each lattice size, oscillations are observed before dipole field cancellation effects causes measurements to settle on a consistent value. Larger structures containing more layers causes greater cancellation, reaching a consistent value of  $|B_{\text{loc}}|$  faster and with fewer oscillations. The effect of non-bulk magnetic moments is also shielded close to the center of larger samples. The results of figure 3 will guide future simulations to make measurements of  $B_{\text{loc}}$  within smaller sub-lattices of a full structure to avoid disrupting edge effects. Additionally, comparison to results quoted in [33] reveals the model produces numerically accurate values of  $|B_{\text{loc}}|$ .

### 3.4 Lattice modelling method and distribution calculations

Having tested the accuracy limit of the direct modelling of dipole fields within a simple structure, the main method for determining  $p(B)$  is now outlined. The parameters of the non-centrosymmetric crystal structure manganese silicide (MnSi) are used for the investigations carried out within this report. MnSi crystallizes in the cubic P2<sub>1</sub>3 space group which is characterized by the absence of a center of symmetry, therefore allowing the material to host a skyrmion lattice [34]. The experimentally determined A-phase for which an SKL phase is stable within MnSi, is used to guide the values of  $B_{\text{ext}}$  chosen for simulations [22]. The simulations performed in this report will only use the parameters associated with a simplified cubic

structure of MnSi in order to generate field strengths of correct magnitude. Hence results are not an accurate generation of the internal field strength of a crystal of MnSi, rather a demonstration of the model ability. The temperature at which simulations are performed is assumed to be  $\approx 29$  K, which allows for the greatest range of  $B_{\text{ext}}$  values to be used for SKL generation. This is because, for this temperature, the A-phase covers a wider range of field strengths [20, 31, 34].

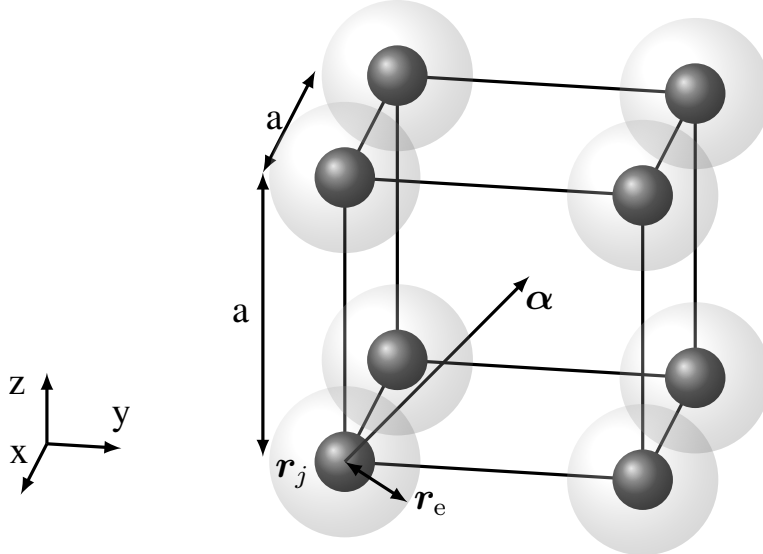


**Figure 4:** Position  $\alpha$ , at which  $|B_{\text{loc}}|$  is measured within each cubic unit cell (depicted). Each solid sphere represents one Mn atom, with the surrounding grey cloud demonstrating an exaggerated measurement exclusion zone. Exclusion spheres are of radius  $r_e = 1 \text{ \AA}$

The aim of the model is to generate a probability distribution  $p(B)$  of the internal magnetic field strengths measured at  $\alpha$ , across a sample lattice. The lattice generation and field calculations have been encoded in Python. A lattice of atoms is first generated. Each atom is located at some Cartesian coordinate of integer components:  $\mathbf{r}_j = (r_x, r_y, r_z)$ . Spin structures are translated onto the atomic lattice positions using equations (14) and (17). From this sample space a sub-lattice of smaller dimensions is then extracted. The extraction of this smaller sample space is motivated by the convergence results of figure 3 and excludes the divergence effects of non-bulk atoms.

The muon stopping point (interstitial site) under investigation is located within each unit cell by adding a vector  $\alpha$  to each atom  $\mathbf{r}_j$ , giving  $\mathbf{r}_i$ . This configuration is demonstrated in figure 4. A single measurement consists of determining  $|B_{\text{loc}}|$  at a randomly chosen  $\mathbf{r}_i$  within the sub-lattice sample, where  $|B_{\text{loc}}|$  is calculated using equation (19). The strength of the dipole field is calculated using all atoms in the extended lattice and equations (20) and (21). To build up each distribution 30,000 measurements are made within the sub-lattice. Results are binned together to produce a continuous histogram representation. The number of bins used to achieve this is set sufficiently high as to capture any profile details and following systematic trial and error was set at 100 bins. The histogram is converted to a probability distribution using the histogram function of the Numpy module in Python. With the density condition set at 'True' [35]. Distributions have been normalised such that  $\int p(B)dB = 1$ . A point on the distribution curve corresponds to

the probability of measuring that field strength within the sample. Performing a cosine Fourier transform on this distribution as dictated by equation (11), allows for a direct mapping of the time evolution of the implanted muon-spin polarization  $P_x(t)$ . To examine distributions of more complex magnetic structures, such as the skyrmion lattice, the spatial variation of  $|B_{\text{loc}}|$  is also calculated by the model. Spatial distributions are determined using periodic calculations of  $|B_{\text{loc}}|$ . Starting from the middle of a skyrmion, measurements are taken along the x and y Cartesian axis in increments of 1 lattice spacing. This provides a means of directly associating a particular field strength to a physical position within a spin texture. The purpose of simulation exercises that will follow is to demonstrate the usage of the model for a very simple cubic structure. The interpretation of resulting distributions will serve as a guide for dissecting future simulations.

The choice of  $\alpha$  depends on which stopping site the method user seeks to study. However, closer to magnetic moments located at the corners of the unit cell, the magnetic field increases as  $r^{-3}$  and hence points close to atom are excluded (exclusion zones are displayed in figure 4). Justification for this comes from Coulomb's law where electrostatic repulsion between a positive muon and cations located at each lattice position makes the probability of a muon stopping close to an atom extremely low [14]. Assuming that muons evenly fill available positions ( $\alpha$ ) then the distribution of muon precession frequencies will exactly follow the distributions of  $p(B)$  [14]. This ability to pick a single interstitial site and determine the expected polarization curve is a particular strength of this direct modelling method.

## 4 Results and discussion of field simulations

Having now described the modelling technique for determining  $p(B)$ , simulations of internal magnetic field distributions generated by the presence of skyrmion lattices will now be presented. In order to interpret distinct features present within  $p(B)$  profiles for a skyrmion lattice, models of FM, AFM, conical and helical spin structures are first generated and discussed. These structures correspond to spin regions found within the skyrmion lattice. The parameters introduced below are applied to all simulations. All spin textures are generated within cubic lattices with lattice spacing  $a = 4.558 \text{ \AA}$  (using a structure analogous to MnSi as before). For each simulation, lattices of dimensions  $200a \times 200a \times 80a$  are generated. Random lattice locations are then taken from a sub-lattice (sample space) of size  $160a \times 160a \times 60a$ . Measurements of  $|B_{\text{loc}}|$  are made at a position  $\alpha = (1.33, 1.93, 1.98)\text{\AA}$  within each unit cell. This particular choice of  $\alpha$  is chosen due to it's low symmetry location within a unit cell. Meaning dipole fields generated by the atoms within the unit cell do not evenly cancel and collapse the  $p(B)$  to a single peak. Magnetic moments of magnitude  $M = 0.4\mu_B$  are used, which is appropriate for the assumed simulation temperature [32].

### 4.1 Probability distributions for FM and AFM structures

First the magnetic field distribution  $p(B)$  is calculated for AFM and FM arrangements of magnetic moments and is displayed in figure 5. Considering  $p(B)$  generated for an AFM structure, as

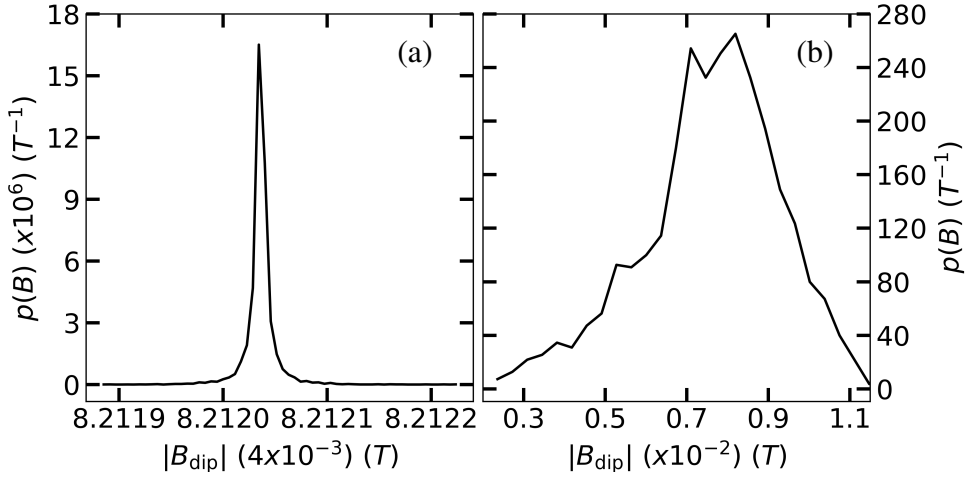


**Figure 5:** Probability distributions of  $B_{\text{loc}}$  within a cubic lattice where spins are arranged: (a) antiferromagnetically (b) ferromagnetically.

observed in figure 5(a), the antiparallel arrangement of neighbouring magnetic moments causes a single symmetrical peak to form. This may be attributed to the cancellation of dipole fields generated by neighbouring magnetic moments. Whilst the magnetic dipole field is long ranged, due to its  $1/r^3$  dependency it is appropriate to consider the dipole field measured at a single point to be dominated by the fields produced by nearest neighbour magnetic moments. An example calculation of the dipole field strength at  $\alpha$  due to a pair of nearest neighbour moments  $m_1 \parallel (0,0,1)$  and  $m_2 \parallel (0,0,-1)$  along a single axis is presented. The dipole field due to the first moment,  $B_{\text{dip},1}$ , at  $\alpha$  is  $(7.1, 12.0, 2.0)$  mT and for the second moment,  $B_{\text{dip},2} = (4.0, -3.0, 2.0)$  mT. The opposite polarities of  $B_{\text{dip}}$  along y results in cancellation of the fields, reducing  $|B_{\text{loc}}|$ . This cancellation effect occurs for fields produced by a pair of magnetic moments of opposite orientation along any axis. Extending the summation to include fields produced by all moments in the sample results in cancellation causing the formation of a single peak.

A similar argument is used to explain the single peak in the FM distribution of figure 5(b). Where dipole fields produced by magnetic moments on neighbouring planes along z will cancel. This is due to neighbouring spin layers, producing fields of opposite polarity once they reach  $\alpha$  [29]. For a large number of layers this will produce a constant measurement field strength. The FM distribution is broader than anticipated but this is likely due to the asymmetrical location of  $\alpha$  within a unit cell. Larger numbers of measurements will solve this broadening. FM and AFM field distributions can be translated to understanding the ferromagnetic region surrounding individual skyrmions. This formation of a single peak due to dipole field cancellation has been experimental observed in [20].

## 4.2 Probability distributions for helical and conical structures

Simulations of field distributions for helical and conical arrangements of magnetic moments are now presented. Helical and conical structures have been generated using a single modulation vector of  $\mathbf{q} = 2\pi/\lambda_{\text{skl}}(1, 0, 0)$  with equation (17). The helical structure is the Bloch wall that was introduced as the basic building block of the skyrmion texture (figure 1(b)) [5].

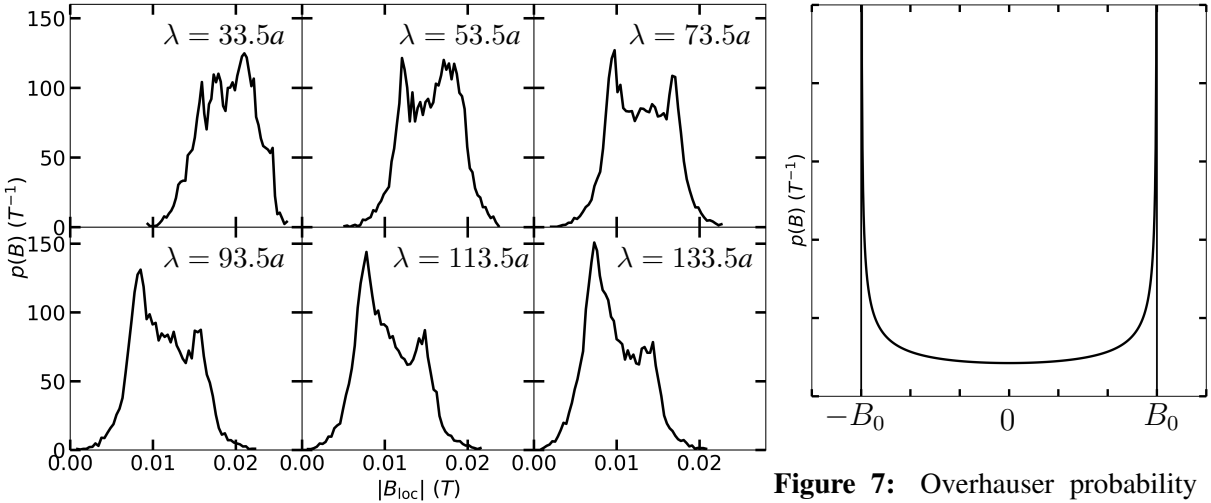


**Figure 6:** Distributions of  $|B_{\text{loc}}|$  measured within helical spin lattices of increasing  $\lambda$ .

**Figure 7:** Overhauser probability distribution for a single  $q$  spin wave in one dimension with  $\lambda \geq a$ . Where  $|B_{\text{loc},\text{max}}| = |B_0|$  [21].

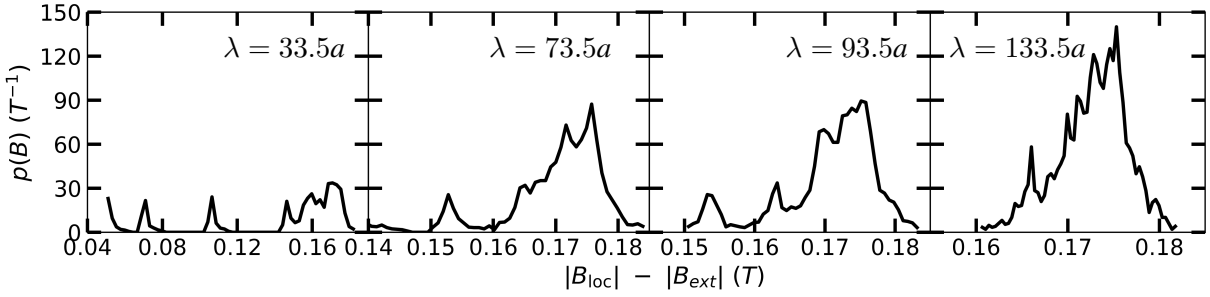


**Figure 8:** Probability distributions with increasing  $\lambda$  for a conical spin structure, using an applied field of  $|B_{\text{ext}}| = 0.24$  T.

Increasing the value of  $\lambda$  has the effect of decreasing the helix rotation periodicity. As peaks and troughs in the field distribution occur where spins rotate more slowly (analogous to the peaks and troughs of a cosine curve), increasing  $\lambda$  causes greater cancellation of generated dipole fields occurs (similar to the FM result). Examining figure 6, as  $\lambda$  increases it is observed that the high field peak (RHS peak) decreases in probability, whilst the peak on the left increases. This change is attributed to greater dipole field cancellation from larger regions of nearly parallel/parallel neighbouring spins (magnetic moments). Therefore increasing the probability of measuring a lower value of  $|B_{\text{loc}}| - |B_{\text{ext}}|$ . The expected  $p(B)$  for a helix is the Overhauser distribution, where the solution for a helical spin wave, producing a spatially varying B-field, is a two peak distribution (figure 7). This provides a means of testing the model against theoretical predictions. As shown in figure 7 two peaks arise from cancellation and reinforcement of dipole fields. The distribution in figure 7 has been calculated for a single dimension, extending to two dimensions will decrease the depth of the central minima. This provides a direct comparison to the lineshape displayed for  $\lambda = 73.5 a$ . Demonstrating the model produces accurate distributions for a helix [21]. Results for a helix can be used to describe the field produced by the rotation of spins across a skyrmion radius.

Now considering field distributions determined for a conical spin structure (figure 1(c)) shown

in figure 8, it is similarly observed that peak splitting and growth depends on the underlying spin rotation periodicity. A slower rotation (with increasing  $\lambda$ ) generates longer regions of near ferromagnetically aligned magnetic moments. For the conical structure this results in field alignment (reinforcement) along the axis of the applied field, causing a single peak to form. The conical spin structure is a phase of the non-centrosymmetric crystal MnSi which occurs when the applied field strength is raised above the A-phase boundaries [34]. Comparing these results to the field distributions obtained for conical spin structure measured using  $\mu$ SR techniques, contributions to the final  $\mu$ SR spectra from several different field strengths is observed. This result points to the presence of smaller peaklets in the field distribution as determined above [36].

### 4.3 Skyrmiion lattice structures

Having used the model to analyse field distributions for simple spin structures, it is now used to determine  $p(B)$  for a skyrmion lattice. The three modulations vectors that are used with equation (17) to generate skyrmion lattices are given as:  $\mathbf{q}_1 = \frac{2\pi}{\lambda_{skl}} (-1, 0, 0)$ ,  $\mathbf{q}_2 = \frac{2\pi}{\lambda_{skl}} \left(\frac{1}{2}, -\frac{\sqrt{3}}{2}, 0\right)$  and  $\mathbf{q}_3 = \frac{2\pi}{\lambda_{skl}} \left(\frac{1}{2}, \frac{\sqrt{3}}{2}, 0\right)$ . With associated azimuthal angles passed to the rotation matrix of:  $\phi_1 = -\frac{\pi}{3}$ ,  $\phi_2 = \pi$  and  $\phi_3 = \frac{2\pi}{6}$  respectively. Values used for  $\lambda_{skl}$  have been guided by literature results, with a range of  $23.5 a \leq \lambda_{skl} \leq 163.5 a$  chosen [22, 32, 34].

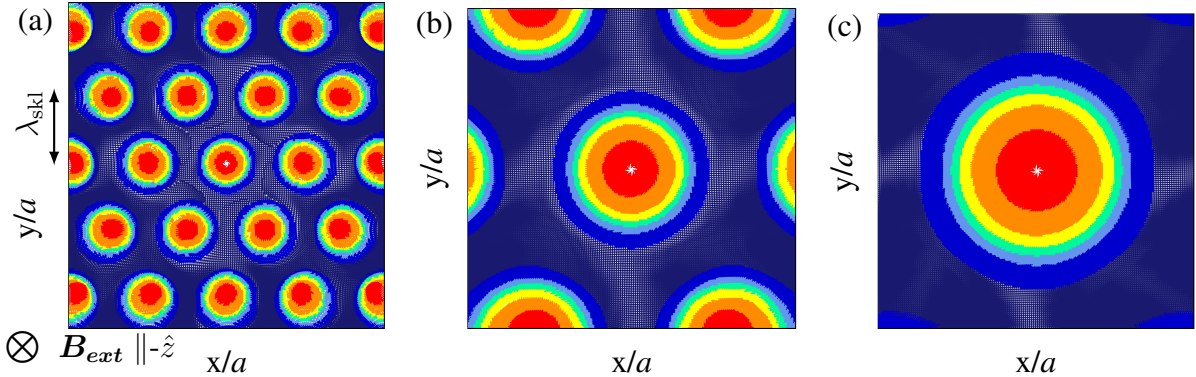


**Figure 9:** Skyrmion lattice spin textures produced with  $B_{ext} \parallel (0, 0, -1) \parallel -\hat{z}$ . Displayed is a sample area of  $120 a \times 120 a$ . The observed coloured spots represent individual skyrmions, separated by a distance of  $\lambda_{skl}$  [22]. Blue regions represent spins aligned along  $+\hat{z}$  and red spins represent individual spins aligned along  $-\hat{z}$ . The intermediate colour gradient between these two maxima represents the helical twisting of spins between  $S \parallel (0,0,-1)$  and  $S \parallel (0,0,1)$  (as in figure 1(a)). (a)  $\lambda_{skl} = 33.5 a$ . (b)  $\lambda_{skl} = 83.5 a$ . (c)  $\lambda_{skl} = 133.5 a$ .

Within MnSi the interplay of various energy scales ( $D$  and  $J$ ) leads to skyrmion spin structures which are incommensurate with the underlying lattice [37]. In order to model this incommensurate texture, non-integer wavelength values of  $\lambda_{skl}$  are used. The hexagonal arrangement of skyrmions in a sample is demonstrated in figure 9. The alignment of  $B_{ext}$  ensures the Zeeman term of equation (6) prevents the skyrmion from unwinding. It is observed that as  $\lambda_{skl}$  is increased the spacing between individual skyrmions increases at a faster rate than  $R_s$ . Hence the inter-skyrmion collinear-ferromagnetic region increases in area. This will prove a key observation for later analysis. Figures 9 and 10 are 2D planar cuts through a sample and so demonstrate

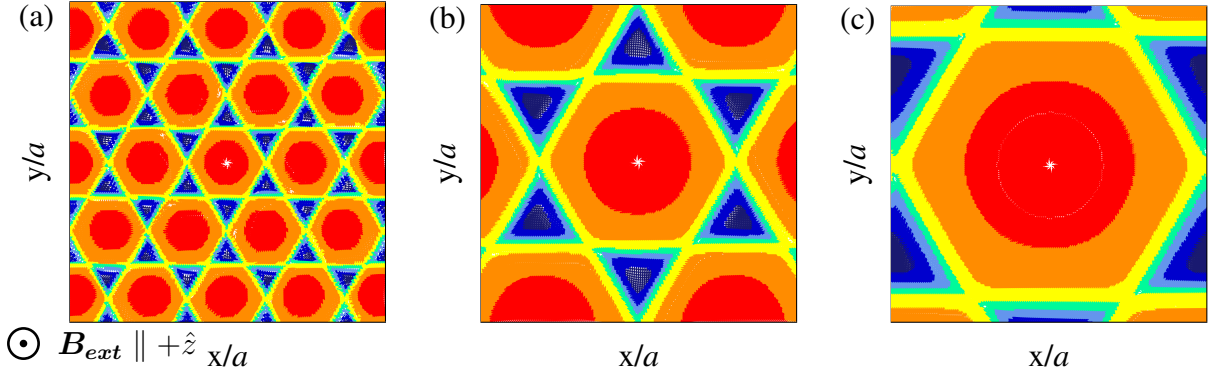


**Figure 10:** Unstable meta-skyrmion spin textures produced with  $B_{ext} \parallel (0, 0, 1) \parallel +\hat{z}$ . The sample size used is  $120 a \times 120 a$ . Blue regions represent spins aligned along  $+\hat{z}$  and red spins represent individual spins aligned along  $-\hat{z}$ . The same colour scheme is used as in figure 1(a). (a)  $\lambda_{skl} = 33.5 a$ . (b)  $\lambda_{skl} = 83.5 a$ . (c)  $\lambda_{skl} = 133.5 a$ .

the arrangement of 3D vortices/tubes which extend along z. Demonstrated in figure 10 is the resulting spin texture if  $B_{ext}$  is rotated in orientation. This does not yield a stable skyrmion phase but provides an interesting spin pattern where the central region of spins aligned along (0,0,-1) grows in size with increasing  $\lambda_{skl}$ . Therefore providing an opportunity to study an entirely different spin texture. The interpretation of  $\lambda_{skl}$  for these structures remains the same in that it determines the separation between nearest neighbour regions of  $S \parallel (0,0,-1)$ . Each individual star shape is deemed as one meta-skyrmion.

#### 4.4 Stable skyrmion lattice field distributions

Field distributions simulated for stable skyrmion lattices ( $B_{ext} \parallel (0, 0, -1) \parallel -z$ ) are first examined. Distributions are produced using a range of applied field strengths, extracted from the stable skyrmion A-phase, of: 0.16 T, 0.20 T and 0.24 T [34]. Additionally an applied field of  $|B_{ext}| = 0.40$  T has been used as an extrema value, that would ordinarily cause a phase transition to a ferromagnetic state [34]. The corresponding skyrmion spin textures used to generate these distributions have the same hexagonal lattice arrangement as observed in figure 9.

Several key observations are made concerning the distributions  $p(B)$  included in figures 11 to 14. Notably the slight 'S'-shape curve stretching between  $\lambda_{skl} = 23.5 a$  to  $\lambda_{skl} = 163.5 a$ . This curve is picked by two main profile features: (a) the decrease in width/increase in height of the central peak and (b) the change in tail length of the distribution and whether the tail stretches to higher/ lower field values.

To examine the described trends, the spatial variation of  $|B_{loc}|$  across a skyrmion lattice is calculated and demonstrated in figure 15. The strong similarities between the distributions shown in figures 11 to 14 means the radial (spatial) distribution will only be demonstrated for one applied field strength but with results applicable to any of the four distributions sets. This is because the same underlying spin texture has been used to model the skyrmion lattice. Increasing  $|B_{ext}|$  acts only to scale the measured of  $B_{loc}$ . Therefore, removing the contribution  $|B_{ext}|$  from the calculation of  $|B_{loc}|$  reveals numerically similar  $p(B)$  profiles. Any slight difference is due

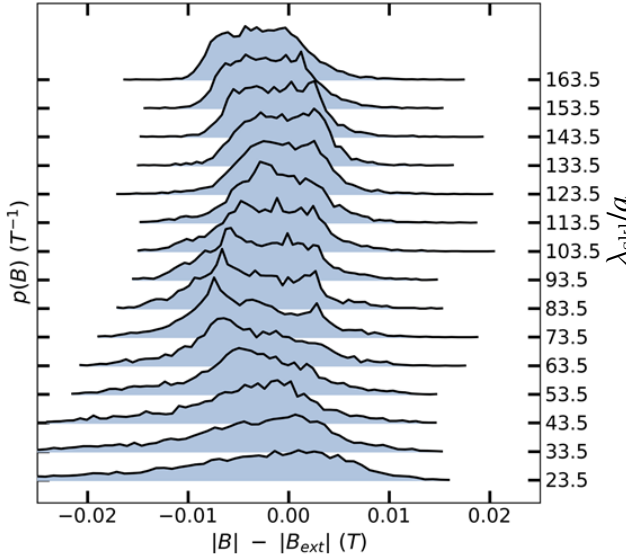


**Figure 11:** Probability distributions for skyrmion lattices of varying  $\lambda_{\text{skl}}$  generated using an applied field of  $\mathbf{B}_{\text{ext}} \parallel (0, 0, -1)$  and  $|\mathbf{B}_{\text{ext}}| = 0.16$  T.

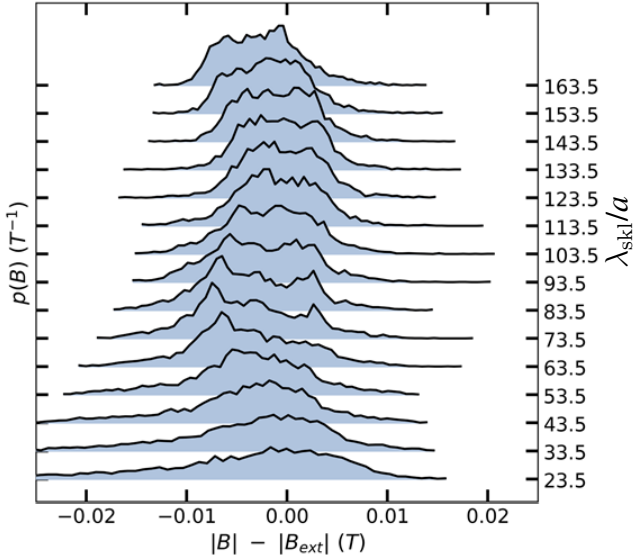


**Figure 12:** Probability distributions for skyrmion lattices of varying  $\lambda_{\text{skl}}$  generated using an applied field of  $\mathbf{B}_{\text{ext}} \parallel (0, 0, -1)$  and  $|\mathbf{B}_{\text{ext}}| = 0.20$  T.

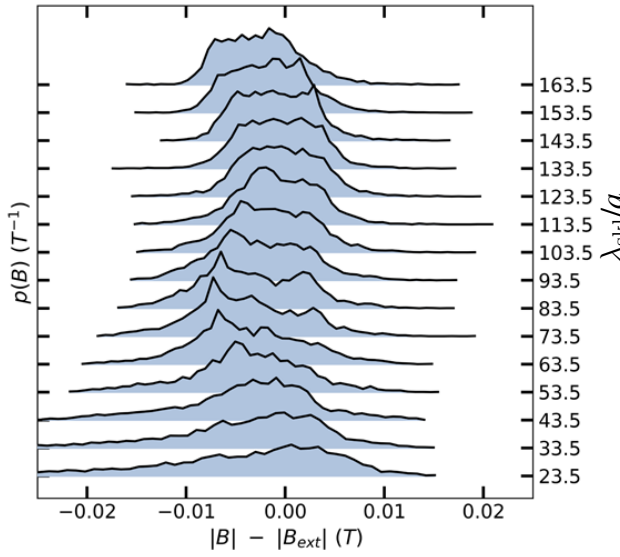


**Figure 13:** Probability distributions for skyrmion lattices of varying  $\lambda_{\text{SKL}}$  generated using an applied field of  $\mathbf{B}_{\text{ext}} \parallel (0, 0, -1)$  and  $|\mathbf{B}_{\text{ext}}| = 0.24$  T.

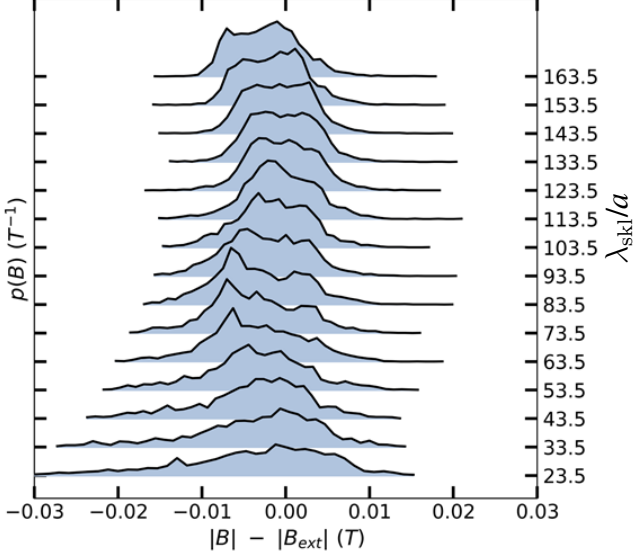


**Figure 14:** Probability distributions for skyrmion lattices of varying  $\lambda_{\text{SKL}}$  generated using an applied field of  $\mathbf{B}_{\text{ext}} \parallel (0, 0, -1)$  and  $|\mathbf{B}_{\text{ext}}| = 0.40$  T.

to noise caused by obtaining  $p(B)$  using random measurements within a non-infinite sample.

Calculated radial distribution curves are demonstrated in sub-plots (e) to (h) of figure 15. Observed in such subplots are periodic peaks and troughs, as measurements pass through individual skyrmions to separating ferromagnetic regions. The initial measurement,  $r = 0$ , is taken at the centre of a skyrmion. The slight deviation between field profiles along x and y is due to the hexagonal arrangement of skyrmions producing different spin structures along each axis. As the skyrmion spacing increases ( $\lambda_{\text{skl}}$ ) the central peak of each distribution becomes sharper (width decreases) and the size of any peak tail decreases in length. The peak value of  $p(B)$

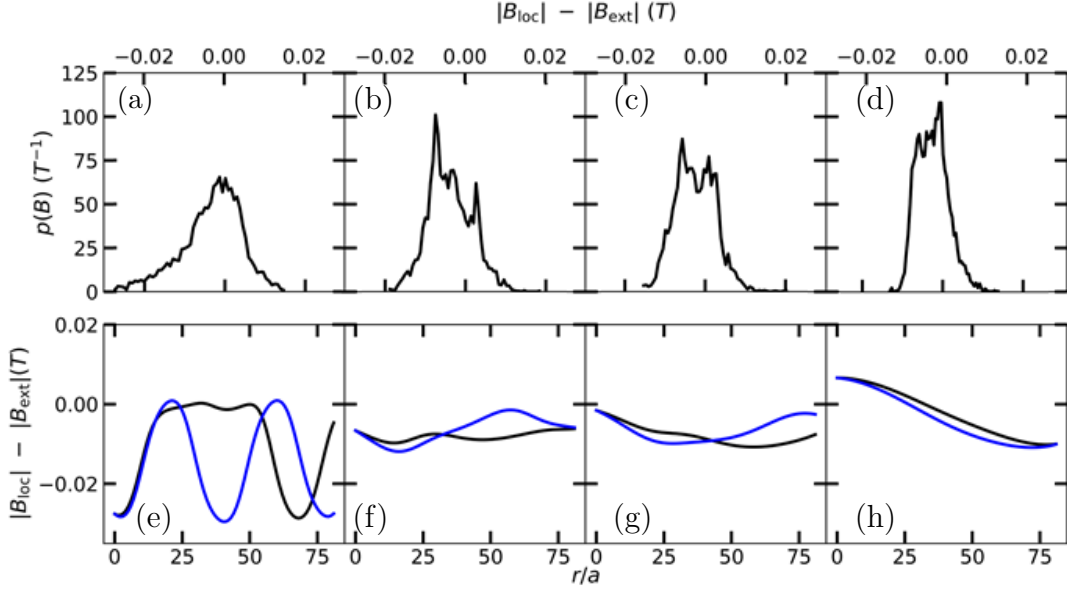


**Figure 15:** Comparison of  $p(B)$  (top panels) against the radial change in  $|B_{loc}|$  with increasing distance  $r$  from the center of a skyrmion (lower panels). The skyrmion lattice has been generated using an applied field of  $|B_{ext}|$  of 0.20 T. Shown in blue are  $|B_{loc}|$  values measured periodically along x and along y in black. Skyrmion wavelengths used: (a),(e)  $\lambda_{skl} = 33.5 a$ , (b),(f)  $\lambda_{skl} = 73.5 a$ , (c),(g)  $\lambda_{skl} = 93.5 a$  and (d),(h)  $\lambda_{skl} = 163.5 a$

determined for each value of  $\lambda_{skl}$  is the most probable field strength measured, indicating the most probable field strength that would be experienced by implanted muons [14]. As was noted earlier, an increase in  $\lambda_{skl}$  causes the inter-skyrmion region of ferromagnetically aligned magnetic moments to increase, as indicated using spins in figure 9. This growing alignment causes increased dipole field cancellation from neighbouring layers of magnetic moments generating a narrower distribution. This is the result that was observed for FM structure. This generates peaks which have centres tending to  $|B_{loc}| - |B_{ext}| = 0$ . This result has been observed experimentally in [32], where measurements made at  $T \geq T_c$  yield an average sample field strength tending to  $|B_{ext}|$ . For this temperature a paramagnetic state exists and moments are observed to ferromagnetically align with  $B_{ext}$ . Within a ferromagnetic region the expected local field approaches 0 and therefore produces a peak in the radial distribution.

The increase in  $\lambda_{skl}$  also causes individual distributions to become skewed to higher values of  $|B_{loc}| - |B_{ext}|$ . This can be attributed to the slight growth of the central spot of ferromagnetically aligned spins along -z (shown in red in figure 9). Dipole fields generated in this central region initially cancel with the applied field. However, from the radial distributions it is observed that increasing  $\lambda_{skl}$  causes field strengths between  $r = 0$  to  $r = R_s$  to increase between (e) to (h). This may be attributed to a growing ferromagnetically aligned region at the centre of each skyrmion, cancelling less with any applied field and instead contributing to the local field strength as dipole fields reinforce one another. Splitting of the central peak is observed between  $\lambda_{skl} \approx 63.5 a$  to  $\lambda_{skl} \approx 123.5 a$ . This is equivalent to the peak splitting observed for a helical structure in figure 6 and is attributed to the slower rotation of magnetic moments across a larger skyrmion radius. Hence peaks are attributed to regions of spins rotating more slowly, such as the central point of

$S \parallel (0, 0, -1)$  and the encapsulating spin texture of  $S \parallel (0, 0, 1)$ .

#### 4.5 Meta-skyrmion lattice field distributions

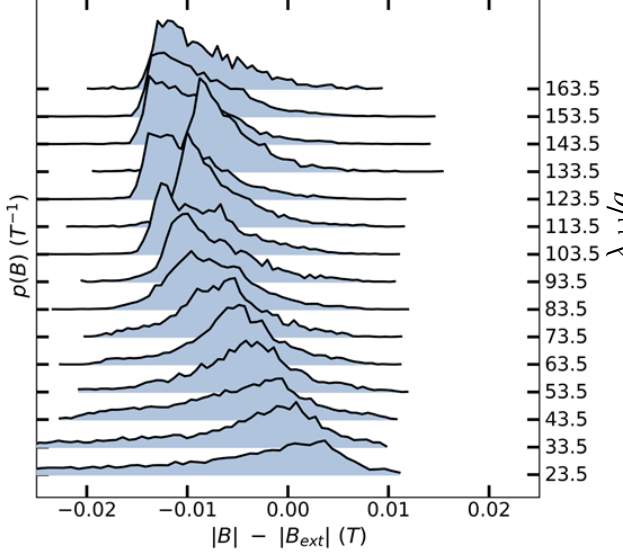


**Figure 16:** Probability distributions for skyrmion lattices of varying  $\lambda_{\text{skl}}$  generated using an applied field of  $\mathbf{B}_{\text{ext}} \parallel (0, 0, 1)$  and  $|\mathbf{B}_{\text{ext}}| = 0.16$  T.

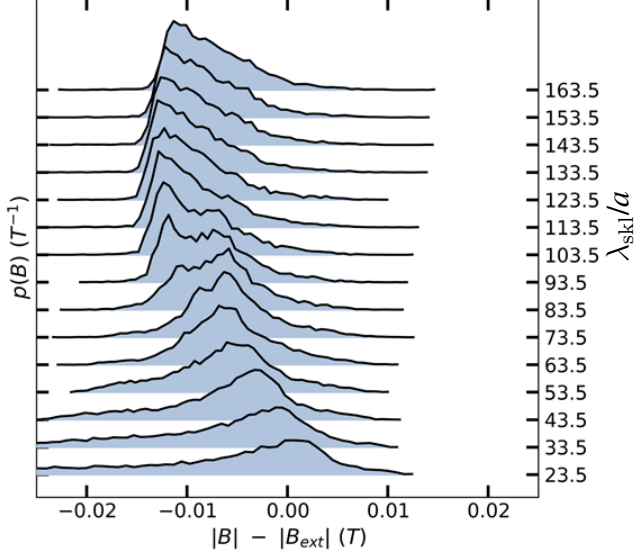


**Figure 17:** Probability distributions for skyrmion lattices of varying  $\lambda_{\text{skl}}$  generated using an applied field of  $\mathbf{B}_{\text{ext}} \parallel (0, 0, 1)$  and  $|\mathbf{B}_{\text{ext}}| = 0.20$  T.

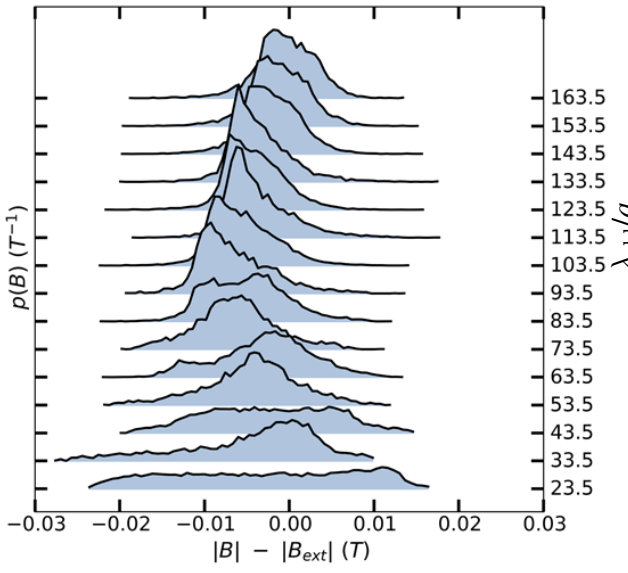


**Figure 18:** Probability distributions for skyrmion lattices of varying  $\lambda_{\text{skl}}$  generated using an applied field of  $\mathbf{B}_{\text{ext}} \parallel (0, 0, 1)$  and  $|\mathbf{B}_{\text{ext}}| = 0.24$  T.

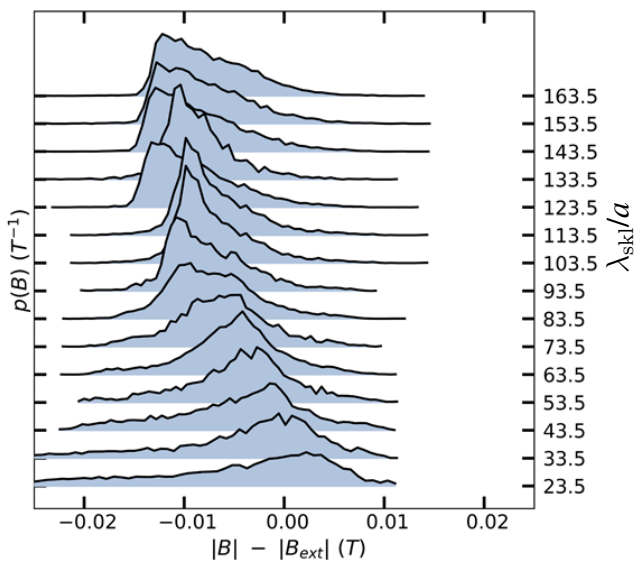


**Figure 19:** Probability distributions for skyrmion lattices of varying  $\lambda_{\text{skl}}$  generated using an applied field of  $\mathbf{B}_{\text{ext}} \parallel (0, 0, 1)$  and  $|\mathbf{B}_{\text{ext}}| = 0.40$  T.

Distributions are now determined for spin structures generated using  $\mathbf{B}_{\text{ext}} \parallel (0, 0, 1) \parallel +z$ , as shown in figure 10. The resulting distributions are included in figures 16 to 19 and have been produced using the same external field strengths as before. The radial change in  $|\mathbf{B}_{\text{loc}}|$  has

been determined for a single external field strength and is included in figure 20. Considering the distributions displayed in figures 16 to 19, two main trends are apparent: (a) the migration of the distribution peak to lower field values and (b) the change from a low field tail to a high field tail. Much of the analysis performed for the previous set of distributions may be similarly applied.

As  $\lambda_{\text{skl}}$  increases, the central region of spins with  $S \parallel (0, 0, -1)$  increases in size (as observed in figure 10). Accompanying this trend is a decrease in  $|B_{\text{loc}}|$  when measured at the center of each meta-skyrmion at  $r = 0$  (shown in subplots (e) to (h)). Employing the same logic as before but with an applied field orientated in the opposite direction, this decrease results from increased cancellation between  $B_{\text{dip}}$  generated by larger regions of ferromagnetically aligned spins and  $B_{\text{ext}}$ . The change from a low field tail to a tail stretching to higher values of  $|B_{\text{loc}}|$  -  $|B_{\text{ext}}|$  is explained using the slower rotation of spins between the regions of  $S_z = -1$  to  $S_z = 1$ . This is demonstrated by the longer, smoother lineshape of 20(h) when compared to 20(e). The smoother curve is observed between  $r = 0$  and  $r \approx \lambda_{\text{skl}}/2$  (analogous to the stable skyrmion radius  $R_s$ ). Sudden changes represent transitions from the meta skyrmion into the surrounding triangles of spins aligned along  $+z$ . A smoother rotation in spins results in more exact cancellation, as was observed for the helical spin structure. Hence a smooth radial change in  $|B_{\text{loc}}|$  -  $|B_{\text{ext}}|$  is observed from low to high values. This produces the sharper peak edges of figures 16 - 19 followed by more distinct high field tails which increase with  $\lambda_{\text{skl}}$ .

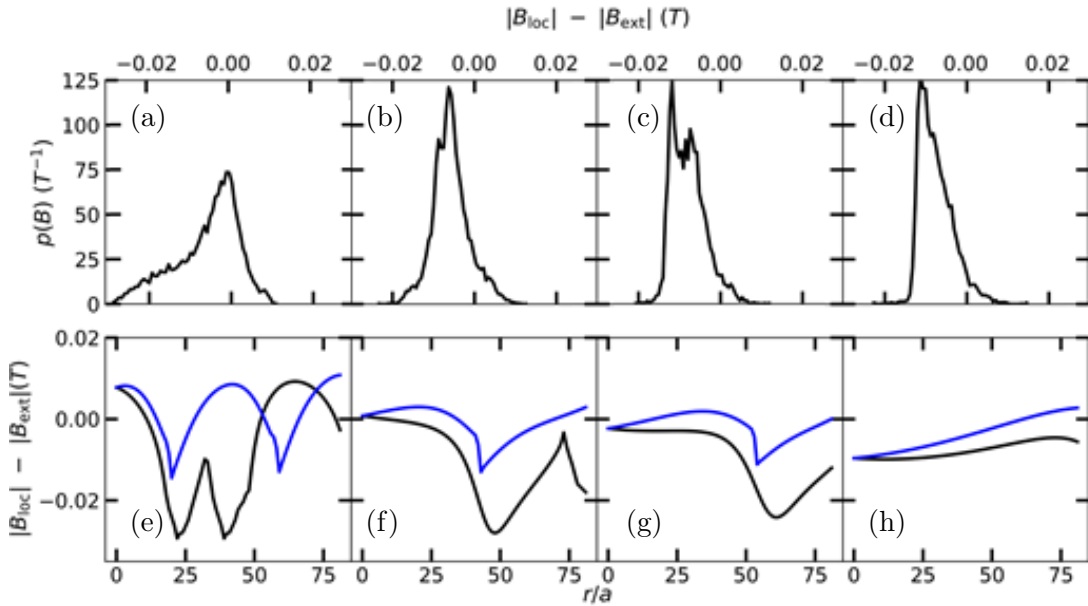


**Figure 20:** Comparison of  $p(B)$  determined for an entire sample lattice (top panels) against the radial change in  $|B_{\text{loc}}|$  with increasing distance  $r$  from the center of a skyrmion (lower panels). Shown in black are  $|B_{\text{loc}}|$  values measured periodically along  $y$  and along  $x$  in blue. Skyrmion wavelengths used: (a),(e)  $\lambda_{\text{skl}} = 33.5 \text{ \AA}$ , (b),(f)  $\lambda_{\text{skl}} = 73.5 \text{ \AA}$ , (c),(g)  $\lambda_{\text{skl}} = 93.5 \text{ \AA}$  and (d),(h)  $\lambda_{\text{skl}} = 163.5 \text{ \AA}$ .

Finally a distribution has been generated with no external field applied (and therefore without the additional vector  $(0, 0, S_z)$  added to the spin texture). The underlying spin texture shown in figure 21 and a field distribution shown in figure 22. Removing the applied field means that the Zeeman energy required to stabilise the skyrmion against unwinding is not provided.

Comparing the widths of the skyrmion particles observed in figure 21 to those observed in figure 9(a), wider skyrmion particles are observed for no applied field. The local field generated by this structure is therefore a result of dipole fields generated by the underlying spin texture only. Analysing the curves of  $p(B)$  included in figure 22 it is observed that the distribution width of the main peak exhibits no discernible change. The broad peak is observed to migrate to lower field values. This may be primarily attributed to a larger FM region at the centre of each skyrmion, causing an increase in dipole field cancellation.

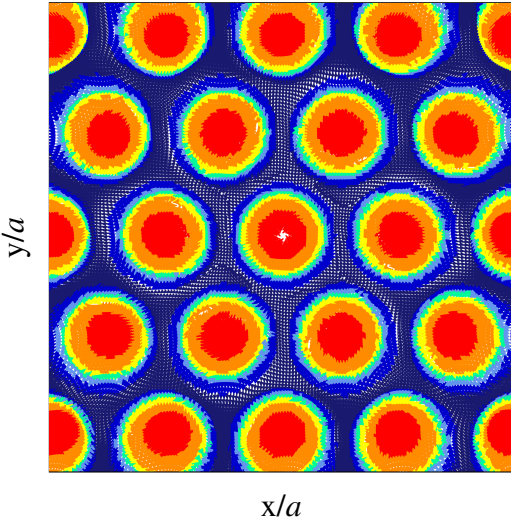


**Figure 21:** Lattice of skyrmion spin structures generated with no applied field. The same colour scheme has been applied as previously used. Individual skyrmions are separated by a distance of  $\lambda_{\text{skl}} = 33.5 a$ .

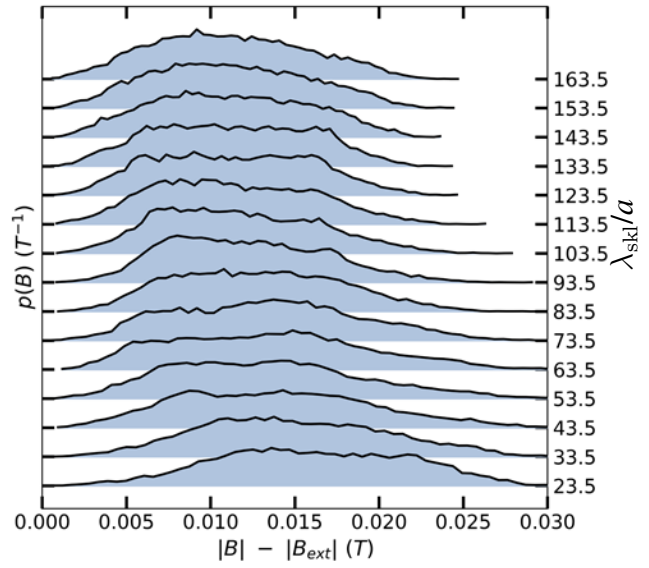


**Figure 22:** Probability distributions for spin textures of varying  $\lambda_{\text{skl}}$  generated using no applied field.

From the results included in figures 11 to 14 and 16 to 19, it has been demonstrated that field distributions can be related to the underlying spin texture using the radial distribution of the  $|B_{\text{loc}}|$ . This is one of the main strengths of the method as it allows for clear connections to be drawn between distribution lineshapes and the underlying field generating spin texture. This type of analysis is difficult using purely experimental results as it requires a knowledge of the local spin texture surrounding each stopping site. However additional spacial imaging of dipole fields should be undertaken. Whilst logical explanations have been presented for the spatial distribution of  $|B_{\text{dip}}|$ , in order for a complete examination of the local field cancellation/reinforcement these distributions should be extended to two dimensions.

## 4.6 Statistical analysis of $p(B)$ distributions

For each of the distributions presented in the last section (figures 11 to 14 and figures 16 to 19) the variance ( $\sigma^2$ ) and skewness (third moment,  $\mu_3$ ) of each distribution  $p(B)$ , is calculated and presented in figures 23(a) and 23(b). The square root of the variance (standard deviation) describes the spread of each distribution about the mean. The skewness measures the degree of distribution asymmetry. A positive value of  $\mu_3$  indicates a distribution with a tail to the right of

the mean (high field tail). A negative value of  $\mu_3$  indicates a tail to the left of the mean (low field tail). A value of  $\mu_3$  close to 0 indicates a symmetrical distribution about the mean [38].

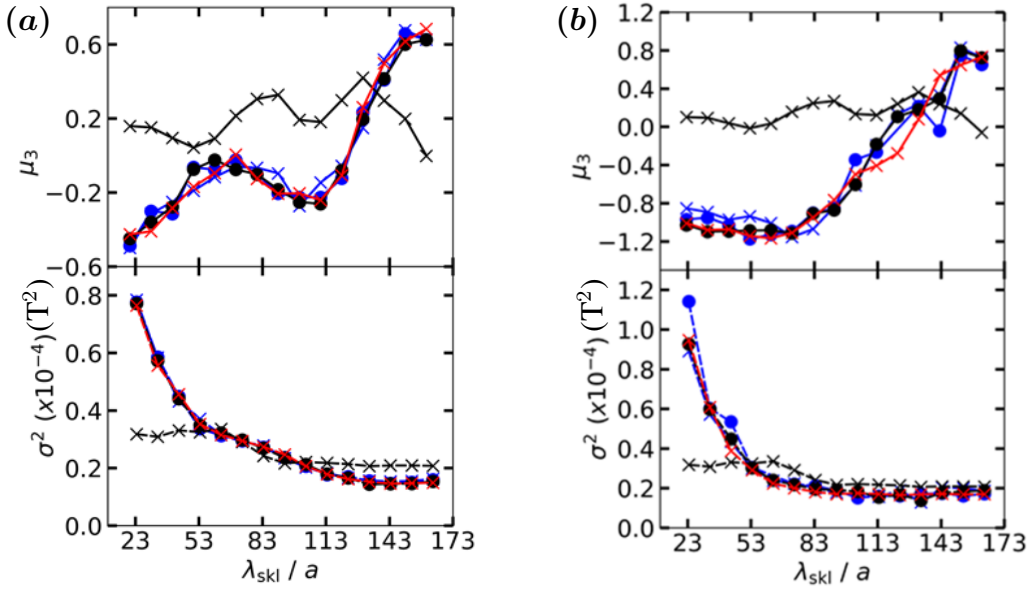


**Figure 23:** (Top panels) Calculated variance,  $\sigma^2$ , of each distribution. (Bottom panels) The skewness,  $\mu_3$ , of each distribution. **(a)** Analysis of  $p(B)$  distributions for skyrmion lattices generated using  $B_{\text{ext}} \parallel (0, 0, -1)$ . **(b)** Analysis of  $p(B)$  distributions for skyrmion lattices generated using  $B_{\text{ext}} \parallel (0, 0, 1)$ . Points represented using a black x have been produced using an applied field of  $|B_{\text{ext}}| = 0$  T, black o using  $|B_{\text{ext}}| = 0.16$  T, red x:  $|B_{\text{ext}}| = 0.20$  T, blue x:  $|B_{\text{ext}}| = 0.24$  T and blue o:  $|B_{\text{ext}}| = 0.40$  T.

Considering first the lower panels of 23(a) and 23(b), the value of  $\sigma^2$  is observed to decrease with increasing  $\lambda_{\text{skl}}$ . This concurs with earlier distribution analysis concerning the decrease in peak width and increase in central peak height as  $\lambda_{\text{skl}}$  increases. Similarly the increase in  $\mu_3$  describes the migration of distribution tails from low to high values of  $|B_{\text{loc}}| - |B_{\text{ext}}|$ . With the 'S'-curve identified in figures 16 to 19 now clearly visible in the trendline of  $\mu_3$ . Plotted results for  $p(B)$  calculated with  $B_{\text{ext}} = 0$  (as indicated in figure 21) yield consistent values of  $\sigma^2$  and sinusoidally varying values of  $\mu_3$  with increasing  $\lambda_{\text{skl}}$ . The uneven growth in skyrmion diameter and the lack of additional cancellation/reinforcement means each distribution maintains a broad spread of field strengths and hence  $\sigma^2$  remains roughly constant. The subtle oscillation of  $\mu_3$  is attributed to the relative growth in the main peak size against peak broadening due to the helical periodicity increasing across the skyrmion radius.

The calculation of these distribution variables is encoded into the method framework and are automatically calculated following the simulation of each distribution. The value of  $\sigma^2$  is used to calculate the expected relaxation rate ( $\Delta$ ) using equation (13). The relaxation rate describes the loss of polarization due to dephasing of the muon ensemble as a result of the inhomogeneous distribution of local fields. The decrease in variance with increasing  $\lambda_{\text{skl}}$  results in a corresponding decrease in relaxation rate (as  $\Delta \propto \sqrt{\sigma^2}$ ). This matches experimentally determined results for the same crystal system quoted in [32], displaying decreasing values of  $\Delta$  as the material transitions from an SKL to ferromagnetic phase. Similar to the increase in ferromagnetically aligned moment regions that were noted earlier. The calculated value of  $\Delta$  is

included in functional descriptions of the muon polarization curve and is discussed later.

As well as demonstrating the application of the model this report seeks to provide a means of interpreting and predicting expected distribution results. Therefore a relationship predicting the variance  $\sigma^2$  of a distribution for a given value of  $\lambda_{\text{skl}}$  is determined. A model of the following form has been fitted to trends observed in the lower panels of figures 23(a) and (b):

$$\sigma^2 = Ae^{-\lambda_{\text{skl}}B} + C, \quad (22)$$

Where A,B and C are fitting parameters which are optimised using a  $\chi^2$  least squares fitting method. An example calculation of parameter optimisations are included in table 1 for the trends shown in figure 23(a).

$ B_{\text{ext}} $	$A (\times 10^{-4})$	$\alpha_A (\times 10^{-4})$	$B (\times 10^{-2})$	$\alpha_B (\times 10^{-2})$	$C (\times 10^{-5})$	$\alpha_C (\times 10^{-5})$
(-0.16) T	1.26	0.09	3.2	0.2	1.5	0.1
(-0.20) T	1.22	0.09	3.1	0.3	1.4	0.1
(-0.24) T	1.34	0.09	3.4	0.3	1.5	0.1
(-0.40) T	1.34	0.09	3.4	0.2	1.6	0.1
Av. & $\alpha_{\text{SD}}$	1.29	0.03	3.22	0.07	1.50	0.03

**Table 1:** Optimised parameters and associated errors ( $\alpha_X$ ) for fits of equation (22) against the trend shown in figure 23(a). Sectioned rows tabulate averages calculated for each parameter and it's associated standard error ( $\alpha_{\text{SD}}$ ).

The parameters included in figure 1 allow for the prediction of distribution variance values without the need for computational simulation. Future users of the model may repeat this approach with appropriate models fit to variance change curves. Then, using equation (13), predictions may be made concerning relaxation rates. This may be used to aid the calibration of positron collection apparatus and experiment timescales.

## 4.7 Calculated polarization signals

Having analysed the field distribution across a skyrmion lattice the final step of the method is a determination of the muon spin polarization evolution with time ( $P_x(t)$ ). Calculated polarization curves are displayed in figure 24. The cosine Fourier transform described in equation (11) is used to calculate each curve using numerical methods obtained from [35]. The timescale over which the polarization evolution is plotted is guided by experimental results [31]. Prior to calculating each curve, the condition that  $|B_{\text{loc}}| \geq 5(\Delta/\gamma_\mu) = \sqrt{\sigma^2}$  must be confirmed before restricting  $P_x(t)$  to a probe of the field along the z axis only. Checking this condition for the lowest applied field strength, results in  $|B_{\text{loc}}| = 0.16 \text{ T} \geq \sqrt{\sigma^2} = 0.02 \text{ T}$ . Hence, only  $p(B)$  along z is probed. A larger range of calculated polarization signals are provided in appendix B. The observed static field distribution solution produces decaying oscillations of a constant angular frequency. These results provide a direct link to the  $\mu$ SR experiment, as figure 24 depicts the signal form that would be expected from plotting the normalised asymmetry of detected positron numbers. The signal is interpreted such that a value of 1 describes a muon polarised along it's original polarization axis (antiparallel to it's original beam momentum) and

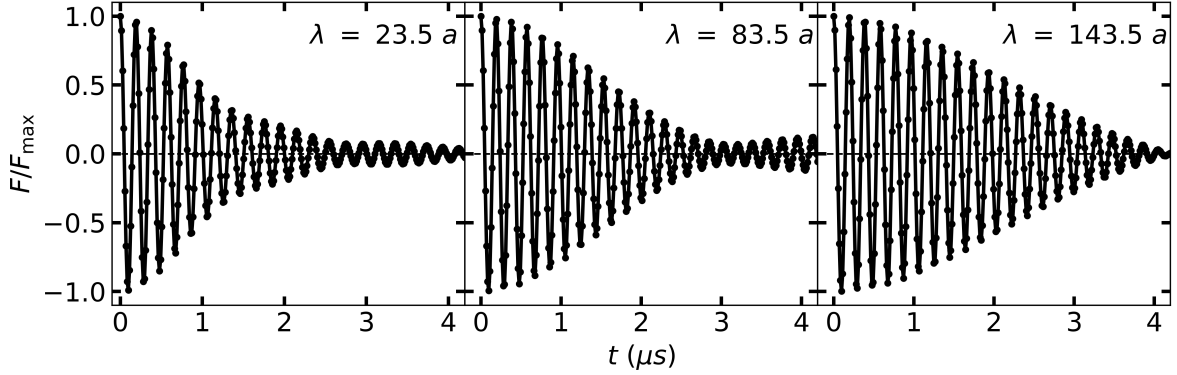


**Figure 24:** The evolution of the muon spin polarization  $P_x(t)$  with time (where  $F/F_{\max}$  is the normalised value of  $P_x(t)$ ). Calculated using  $p(B)$  for skyrmion lattices generated using  $B_{\text{ext}} \parallel (0, 0, -1)$  and  $|B_{\text{ext}}| = 0.24$  T. The polarization function within each panel has been calculated using  $p(B)$  of the indicated  $\lambda_{\text{skl}}$

a value of  $-1$  indicates a muon spin rotation of  $\pi$  about  $z$ . Hence the average ensemble spin,  $\langle S_\mu(t) \rangle$ , is shown to precess with time, periodically passing through each configuration. It is mathematically predicted that the cosine Fourier transform of a Gaussian distribution produces a Gaussian envelope. Such Gaussian envelopes are of the form observed for the  $\lambda_{\text{skl}} = 143.5 \text{ \AA}$  polarization curve. Hence as modelled distributions  $p(B)$  tend towards a single symmetrical peak, the polarization curve approaches the expected envelope [39]. It is therefore appropriate to conclude that the model successfully predicts the time evolution of the muon polarization when compared to theoretical predictions. This result is the main success of the method as it demonstrates that by determining  $p(B)$ , then the polarization curves can be predicted to a good degree of accuracy. Even when using only approximate parameters.

From  $\sigma^2$  determined for distributions displayed in figure 24, the relaxation rate ( $\Delta$ ) decreases as the variance of the distribution decreases. As the relaxation rate describes the tapering of the envelope surrounding the oscillations, a smaller value of  $\Delta$  indicates a slower loss of polarization and hence smaller oscillation damping. This is observed in figure 24 by the slower envelope tapering between  $\lambda_{\text{skl}} = 23.5 \text{ \AA}$  to  $143.5 \text{ \AA}$  [21]. This is a direct result of larger ferromagnetically arranged regions of spins for larger  $\lambda_{\text{skl}}$  skyrmion arrangements. This causes  $B_{\text{loc}}$  to become primarily concentrated along  $+\hat{z}$  and therefore more of the spin rotation is concentrated around the  $z$ -axis. The decay of the distributions depicted in figure 24 is suggestive of any functional form of  $P_x(t)$  having some dependency of the form  $\exp(-\Delta^2 t^2/2)$ . Representing the damping of oscillations as a result of inhomogeneous sample field distributions [21, 39].

The smooth Gaussian-like envelopes displayed in figure 24 differ from experimentally determined data [36]. This is because experimentally determined signals feature a superposition of muon polarization curves. To produce accurate predictions of  $\mu$ SR signals for a sample crystal a superposition of precession signals should be calculated using all possible muon stopping sites. For the simple simulations presented in this report only a single stopping site is considered and therefore limits direct comparison to experimental results. Constructing this superposition solves the main limitation of the  $\mu$ SR experiment. As once a direct comparison to an experimentally determined  $\mu$ SR signal is achieved, the field distributions modelled for each constituent stopping site provide a clear description of the internal field of the physical sample.

## 5 Method evaluation

Using the model framework to calculate  $p(B)$  for skyrmion and meta skyrmion spin structures has been demonstrated to produce distributions comparable to experimentally determined results (with differences dependent on exact experimentally geometry and any simplifications made in this report). This demonstrates the method as a viable means of linking experimentally observed profile features to the underlying physical magnetisation causing them. Furthermore, it has been discussed how polarization signals from several muon stopping sites can be combined in a superposition to give a  $\mu$ SR spectra with a signal form resulting from several known stopping sites. Thus solving the main limitation of the  $\mu$ SR experiment by distinguishing between signal contributions made by individual stopping sites [14]. Without any prior information of stopping sites, the above method could be applied to determine such sites through intelligent trial and error of  $\alpha$ , followed by subsequent comparison of simulated distributions to experimentally determined spectra. Adding the calculation of a fast Fourier transform (FFT) of  $P_x(t)$  would aid this strategy by revealing angular frequency contributions ( $\omega$ ) arising from the field inhomogeneity [2]. This may prove a useful comparison when dissecting a  $\mu$ SR signal for a muon ensemble embedded across several interstitial locations [14, 31]. For example, four distinct precession frequencies in the  $\mu$ SR spectra from muons embedded in MnSi, points to stopping at the 4a Wyckoff position [32].

One advantage of the model is the ease with which different crystal structures may be generated. For crystals constructed from unit cells of several different atoms the model offers an easy way to tackle this scenario. Each individual unique constitute atom of the unit cell may be represented as a sub-lattice with lattice constant equal to the spacing between equivalent atoms in adjacent unit cells. Now restricting each sub-lattice to the same coordinate system, the final unit cell is constructed by adding a vector offset equal to the exact position of each atom within a unit cell. In this way it is easy to define complex systems such as ferrimagnetic systems where each atom possesses a different magnetic moment [27]. A variety of different spin structure may also be constructed. For the specific case of skyrmion spin textures, equation 17 may be easily used to generate a Néel skyrmion by changing  $\hat{e}_i$  to lie parallel to  $\mathbf{q}_i$  [5]. Or a square lattice skyrmion state which is generated using two modulation vectors directed perpendicular to one another and confined to a single plane [22].

Whilst the strength of the model has been discussed, there are several improvements that may be made to increase the accuracy further. The first inclusion is the hyperfine contact term into equation (19). This contribution to the local magnetic field strength has been excluded from the simplified example discussed in this report but should be included to give the model wider applicability (in particular to metallic structures). The hyperfine term includes the contribution to the local field from the overlap of the muon wavefunction and conduction electrons at the stopping site [29]. The second improvement concerns the perturbation of the host crystal environment surrounding a muon stopping site. This perturbation results from magnetic dipolar coupling between the muon spin and the nuclear spin of a neighbouring ion. The result of this interaction depends on the geometry of the bound state formed between the muon and its host and also the individual charges of all parties involved in the interaction. The interaction results

in displacement of individual atoms from their equilibrium positions, which in turn affects the dipole field produced [24]. Such a perturbation may be encoded into the model described in this report by an offset vector representative of the experienced perturbation to individual atom positions  $\mathbf{r}_i$ . The inclusion of stated improvements should be at the discretion of the experimenter and the desired accuracy achievements. Future work should be centered on testing the limits of the model by choosing different stopping sites to those discussed in this report as well as modelling a larger variety of skyrmion types.

## 6 Conclusions

This paper has demonstrated a method for calculating the expected polarization signal generated by a sample in a TF  $\mu$ SR experiment. This signal was determined by performing cosine Fourier transforms of simulated internal magnetic fields. Polarization signals were obtained using the non-trivial field distributions arising from the presence of Bloch skyrmion lattices. These distributions were analysed by first considering distributions arising from ferromagnetically and antiferromagnetically arranged magnetic moments, before progressing to helical and conical structures. This paper may therefore be considered a partial guide on drawing links between simulated distribution lineshapes and the underlying field generating spin structure. It was demonstrated that an increase in dipole field cancellation with increasing inter-skyrmion ferromagnetic spin regions resulted in distribution peaks of exponentially decreasing variance. This resulted in decreasing relaxation rates causing polarization oscillations to experience decreased damping.

The ability of the method to solve one of the most limiting factors of  $\mu$ SR experimental methods has also been discussed. For a known set of stopping sites or using theoretically predicted sites, the exact sample polarization function as a superposition of all sites may be determined. Comparison between predicted and measured polarization signals is a quick and simple strategy of checking the accuracy of these stopping sites. It also provides a means of uncovering any unforeseen structural perturbations or experimental mis-calculations.

This paper therefore lays the groundwork for the development of a more complete Python program capable of predicting field distributions for a range of simulated magnetism phases and across a range of host crystal structures. The main advantage held by the presented method over established programs is it's simplicity and versatility. Few programs exist which give the user full control over the arrangement of atoms and the type of spin structure within a material. Given the limited number of muon spectroscopy facilities worldwide, a detailed and accurate simulation would allow experimenters to predict and plan experiments without access to physical sites.

## 7 Acknowledgements

I would like to thank my supervisor professor Tom Lancaster for his continued support and guidance throughout the project.

# Bibliography

- [1] R. L. Garwin, L. M. Lederman & M. Weinrich, *Observations of the Failure of Conservation of Parity and Charge Conjugation in Meson Decays: the Magnetic Moment of the Free Muon*, Phys. Rev. (1957) **105** 1415
- [2] A. Amato, *Heavy-fermion systems studied by SR technique*, Rev. Mod. Phys. (1997) **69** 1119
- [3] S. J. Blundell, *Spin-polarized muons in condensed matter physics*, Con. Phys. (1999) **40** 175
- [4] P. Dalmas de Reotier & A. Yaouanc, *Muon spin rotation and relaxation in magnetic materials*, J. Phys. Cond. Matt. (1997) **9** 9113
- [5] T. Lancaster, *Skyrmions in magnetic materials*, Con. Phys. (2019) **60**(3) 246
- [6] T. H. R. Skyrme, *Unified field theory of mesons and baryons*, Nucl. Phys. (1962) **31** 556
- [7] J. Hoon Han, *Skyrmions in Condensed Matter*, Berlin, Springer (2017)
- [8] A. N. Bogdanov & D.A. Yablonskii, *Thermodynamically stable vortices in magnetically ordered crystals. The mixed state of magnets*. Sov. Phys. JETP (1989) **68** 101
- [9] F. Büttner et al., *Theory of isolated magnetic Skyrmions: from fundamentals to room temperature applications*, Nature (2018) **8** 4464
- [10] J. Hagemeister et al., *Stability of single skyrmion bits*, Nat. Commun. (2015) **6** 8455
- [11] C. Hanneken et al., *Electrical detection of magnetic skyrmions by tunneling non-collinear magnetoresistance*, Nature Nanotech (2015) **10** 1039
- [12] A. Fert, V. Cros and J. Sampaio, *Skyrmions on the track*, Nature Nanotech (2013) **8** 152
- [13] A. K. Nayak et al., *Magnetic antiskyrmions above room temperature in tetragonal Heusler materials*, Nature (2017) **548** 561
- [14] S. J. Blundell, *Dipole-field distributions in complex magnetic materials*, Physica B (2009) **404** 581
- [15] A. O. Leonov and M. Mostovoy, *Multiply periodic states and isolated skyrmions in an anisotropic frustrated magnet*, Nature (2015) **6** 8275
- [16] T. Arai, *Exchange Interaction and Heisenberg's Spin Hamiltonian*, Phys. Rev. B (1962) **2** 126
- [17] W. Jiang et al., *Skyrmions in magnetic multilayers* Phys. Reports (2017) **704**(23) 1
- [18] E. Balkind, A. Isidori and M. Eschring, *Magnetic skyrmion lattice by the Fourier transform method*, Phys. Rev. B (2019) **99** 134446
- [19] S. Mühlbauer et al., *Skyrmion Lattice in a Chiral Magnet*, Science (2009) **323**(5916) 915
- [20] T. Lancaster et al., *Transverse field muon-spin rotation signature of the skyrmion-lattice phase in Cu<sub>2</sub>OSeO<sub>3</sub>*, Phys. Rev. B (2015) **91** 224408
- [21] P. D. de Réotier et al., *On the Robustness of the MnSi Magnetic Structure Determined by Muon Spin Rotation*, Quantum Beam Sci. (2018) **2** 19

- [22] T. Nakajima et al., *Skyrmion lattice structural transition in MnSi*, Sci. Adv. (2017) **3** e1602562
- [23] R. Takagi et al., *Particle-Size dependent structural transformation of skyrmion lattice*, Nat. Commun. (2020) **11** 5685
- [24] Y. Kakehashi et al., *Multiple Helical Spin Density Waves and Magnetic Skyrmions in Itinerant Electron Systems*, J Phys. Soc. Japan (2018) **87** 9
- [25] G. Arfken *Mathematical Methods for Physicists*, 3rd ed. Academic Press, Florida (1985) pages 198-200
- [26] G. Wysin, *Magnetic Excitations and Geometric Confinement: Theory and Simulations*, IOP Publishing - eBook (2015)
- [27] S. J. Blundell, *Magnetism in Condensed Matter Physics*, Oxford, Oxford University Press (2001)
- [28] J. S. Möller et al., *Quantum states of muons in fluorides*, Phys. Rev. B (2013) **87** 121108(R)
- [29] D. C. Johnston, *Magnetic dipole interactions in crystals*, Phys. Rev. B (2016) **93** 014421
- [30] P. D .Hatton et al., *Real-space imaging of confined magnetic skyrmion tubes*, Nat. Comms. (2020) **11** 1726
- [31] A. Amato et al., *Understanding the  $\mu$ SR spectra of MnSi without magnetic polarons*, Phys. Rev. B (2014) **89** 184425
- [32] T. Lancaster et al., *Transverse field muon-spin rotation measurement of the topological anomaly in a thin film of MnSi*, Phys. Rev. B (2016) **93** 140412(R)
- [33] R. De Renzi et al., *Magnetic properties of  $MnF_2$  and  $CoF_2$  determined by implanted positive muons. I. Localization studies*, Phys. Rev. B (1984) **30** 186
- [34] T. Yu Ou Yang et al., *Manganese Deficiency in MnSi Single Crystal and Skyrmion Pinning*, IEEE Trans. on Magn. (2014) **50** 11
- [35] Q. Kong, T. Siauw & A. Bayen, *Python Programming and Numerical Methods: 1st Edition*, Academic Press, Cambridge MA (2020)
- [36] P. D. de Réotier, *Unconventional magnetic order in the conical state of MnSi*, Phys. Rev. B (2017) **95** 180403(R)
- [37] R. Georgii & T. Weber, *The Helical Magnet MnSi: Skyrmions and Magnons*, Quantum Beam Sci. (2019) **3**(1) 4
- [38] C. Forbes, M. Evans, N. Hastings & B. Peacock, *Statistical Distributions: Fourth Edition*, John Wiley & Sons, New Jersey (2011)
- [39] A. Amato, *Physics with Muons: From Atomic Physics to Solid State Physics*, University of Zürich, February 2019, Lecture series - PHY 432
- [40] P.Virtanen et al., *SciPy 1.0: Fundamental Algorithms for Scientific Computing in Python*, Nat. Meth. (2020) **3** 17

## Appendix A. Error Analysis

This Appendix will examine the techniques used to determine the errors quoted in the main report body. All techniques and methods are taken from, *Measurements and their Uncertainties* by I.G.Hughes and T.P.A.Hase, published by *Oxford University Press* (2010). All of the methods of error evaluation described in this section are completed in Python coding and make use of several NumPy functions but with raw operations within modules still following the described methods.

The variance values included in figure 23(a) and (b), are calculated using the following equation:

$$\sigma^2 = \sum_{i=1}^N d_i^2 \frac{1}{N-1}, \quad (\text{A1.1})$$

where  $N$  is the number of measurements taken during the profile mapping and  $d$  is the difference between the average magnetic field strength and each individual measurement. This quantity describes the spread of the data around the average value of the distribution. The third moment ( $\mu_3$ ) is also displayed in these figures and is a measure of the skewness of the data set. Skewness is defined as the expected value (E) of:

$$\mu_3 = E \left[ \left( \frac{X - \bar{B}}{\sigma} \right)^3 \right]. \quad (\text{A1.2})$$

Where  $\bar{B}$  is the average magnetic field strength of a distribution.  $\sigma$  is the standard deviation (square root of the variance). The value  $X$  is an individual field strength.

In order to produce the fit parameters displayed in table 1 and used to optimise equation (22), a  $\chi^2$  squared least fitting method was used. This technique was automated in Python code and uses the *scipy.optimize.CurveFit* package from the Scipy module to complete the iterations. The *scipy.optimize.CurveFit* package uses a Marquardt-Levenberg (ML) algorithm to complete the optimisation [40]. The ML algorithm uses the method of steepest descent to first minimise trial parameters and then once parameters approach a minimum value of  $\chi^2$  (i.e any following change in fitting parameter values increases  $\chi^2$ ) on an error surface, the algorithm switches to an expansion method. The value of  $\chi^2$  is calculated using:

$$\chi^2 = \sum \frac{(y_i - y(\lambda_i))^2}{\alpha_i^2}. \quad (\text{A1.3})$$

Where the value of the error bars  $\alpha_i$  are set as 1, meaning that  $\chi^2$  is dependent only on the difference between the  $y_i$  i-th data point on the variance curves seen in figure 23 and the variance value ( $y(\lambda_i)$ ) calculated using equation (22) for the corresponding value of  $\lambda_i$ .

The error surface is defined by contours of constant  $\chi^2$  on an  $N$  dimensional surface. The gradient descent method sees the algorithm minimise each parameter until it reaches a central point on the error surface which is a minimum value of  $\chi^2$ . With each axis defined by increments of a single parameter. Each parameter,  $\alpha_j$ , is simultaneously varied by a small amount,  $\delta\alpha_j$ , such

that the gradient:

$$(\nabla \chi^2)_j = \frac{\partial \chi^2}{\partial a_j} \approx \frac{\chi^2(a_j + \delta a_j) - \chi^2(a_j)}{\delta a_j}, \quad (\text{A1.4})$$

points along the direction in which the surface varies most rapidly. Therefore tending to the central minimum much faster. As the error surface is parabolic around the local minimum (central minimum) therefore a Taylor-Series expansion (expansion method) of equation (A1.4) can be used to describe the error surface. As part of this second order expansion the  $N \times N$  matrix known as the Hessian matrix is generated. Where  $N$  gives the number of parameters being minimised. Taking factors of 2 out from the Hessian matrix (multiplying by  $\times 1/2$ ) produces the curvature matrix. The curvature matrix is defined as

$$A_{jk} = \frac{1}{2} \frac{\partial^2 \chi^2}{\partial a_j \partial a_k}. \quad (\text{A1.5})$$

The off diagonal terms of the matrix describe the curvature of the  $\chi^2$  along directions that are not parallel with a parameter axis. Taking the inverse of this matrix produces the error matrix  $C$ :

$$[C] = [A]^{-1}. \quad (\text{A1.6})$$

Where the off diagonal terms give the statistical error in each of the fitting parameters. The associated error for each parameter ( $a_j$ ) is therefore defined as

$$\alpha_j = \sqrt{C_{jj}}, \quad (\text{A1.7})$$

which describes the instance where increasing the parameter in question by  $\alpha_j$  causes the value of  $\chi^2_{min}$  to increase to  $\chi^2_{min} + 1$  on the error surface.

Within table 1 the average parameter value is also presented using the standard error of each set of parameters. The standard error is defined as:

$$\alpha = \frac{\sigma}{\sqrt{N}} \quad (\text{A1.8})$$

where  $\sigma$  is the standard error and is calculated using the square root of equation (A1.1). And  $N$  is the number of data sets, in this case 3.

## Appendix B. Additional polarization Curves

Included within this appendix are additional polarization signals which have been calculated for applied field strengths of  $|B_{\text{ext}}| = 0.24$  T. The corresponding field distributions  $p(B)$  which have been used to calculate these curves are shown in figures 13 and 18 within the main text respectively.

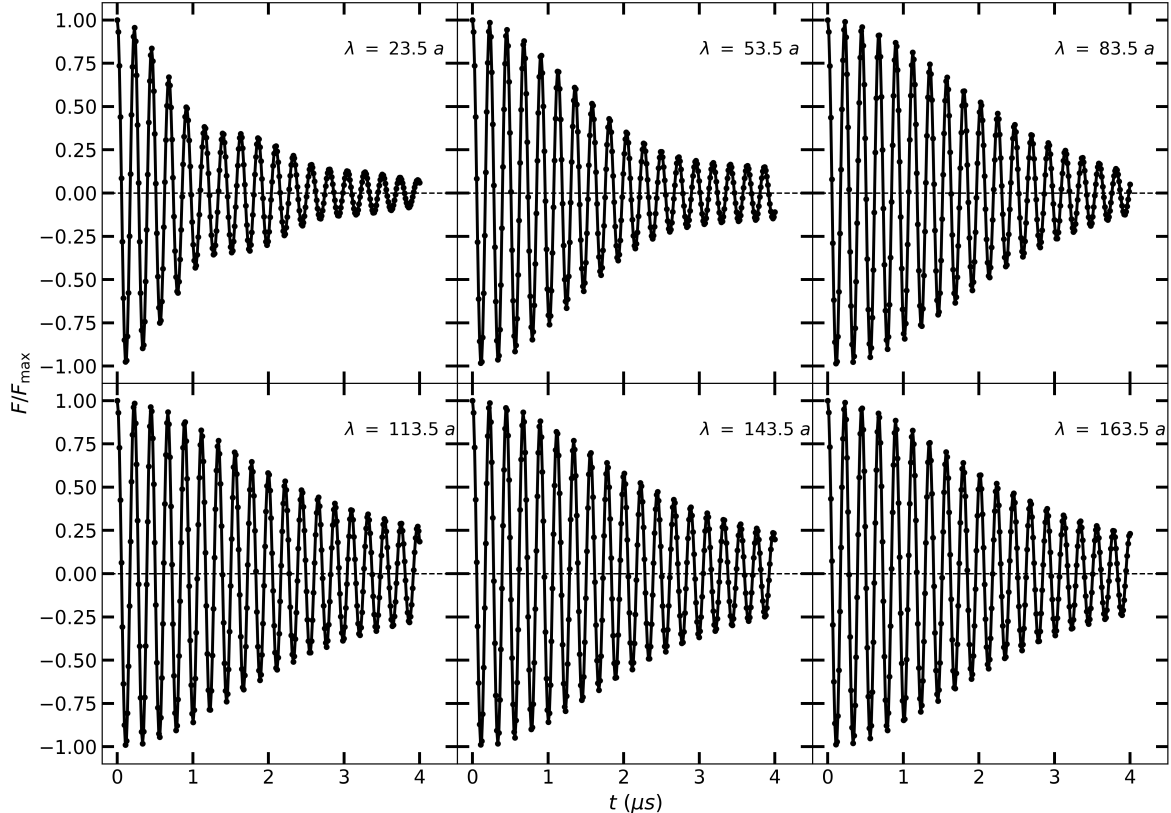


**Figure 25:** The evolution of the muon spin polarization curve  $P_x(t)$  with time. Calculated using  $p(B)$  distributions for skyrmion lattices generated using  $B_{\text{ext}} \parallel (0,0,-1)$  and  $|B_{\text{ext}}| = 0.24$  T. The polarization function within each panel has been calculated using the distribution of the indicated value of  $\lambda_{\text{skl}}$ . Where  $F/F_{\text{max}}$  is the normalised value of  $P_x(t)$

The inclusion of these figures serves to further demonstrate the tapering of the oscillation envelope with increased  $\lambda_{\text{skl}}$ . The trend for both orientations of  $B_{\text{ext}}$  is for the distribution variance to decrease with increasing  $\lambda_{\text{skl}}$ , hence a similar tapering result is observed for both orientations. The faster decay decrease for positive field alignments over this range represents the faster decrease in variance.

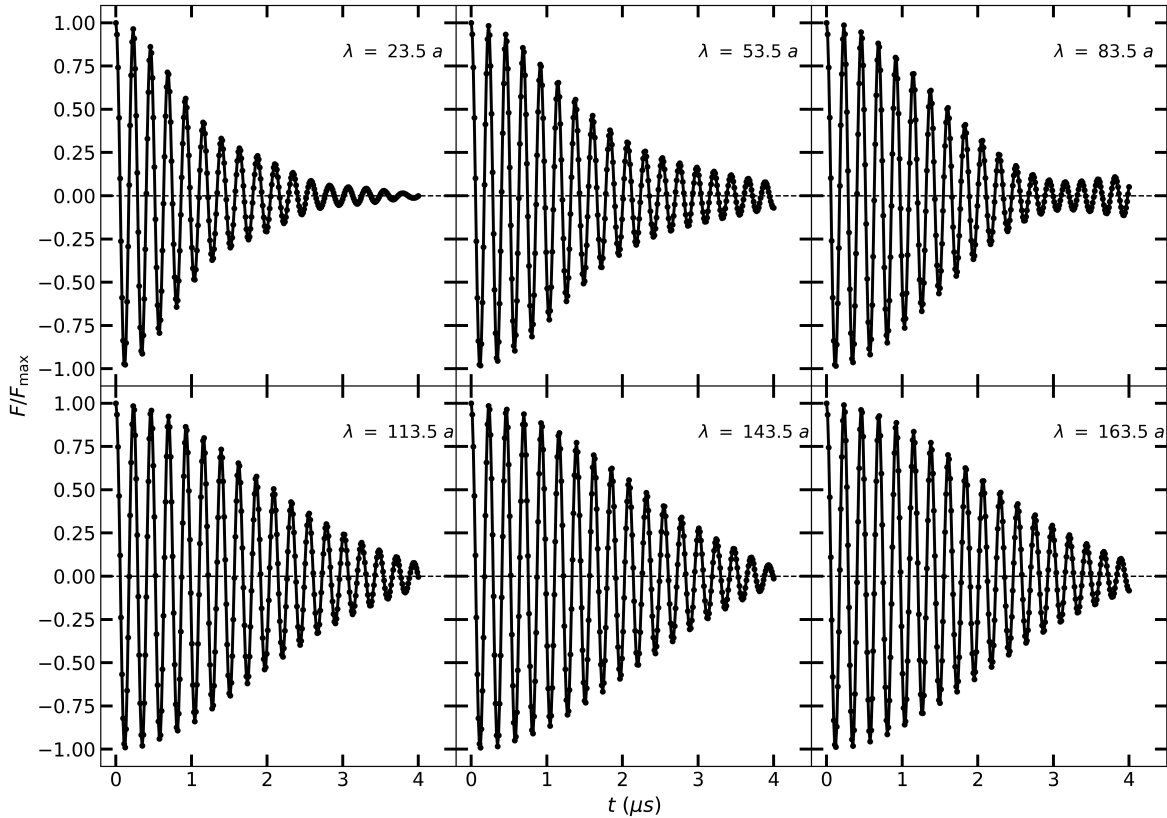


**Figure 26:** The evolution of the muon spin polarization curve  $P_x(t)$  with time. Calculated using  $p(B)$  distributions for skyrmion lattices generated using  $B_{\text{ext}} \parallel (0,0,1)$  and  $|B_{\text{ext}}| = 0.24$  T. The polarization function within each panel has been calculated using the distribution of the indicated value of  $\lambda_{skl}$ . Where  $F/F_{\max}$  is the normalised value of  $P_x(t)$

## Appendix C. Python code: $p(B)$ modelling code

Within this section a simplified version of the code that has been used to calculate the skyrmion lattice field distributions is included. This code only shows the basic functions and does not include any plotting commands. Additionally elements such as automatic saving have been removed to leave behind only the raw method code. This code therefore constitutes a small part of the code. All numerical methods performed on the results of this code are described in full in the main text.

---

```
Skyrmion.py
import numpy as np
import matplotlib.pyplot as plt
import datetime as datetime
import math
import random

"""
Script to determine the magnetic field distribution within a
skyrmion lattice
"""

spinmag = 0.4*9.274010e-24
mu_0 = 4e-7*np.pi
mu_B = 9.274010e-24
sep = 4.558e-10

def Rot_Mat(phi, theta, psi, r):

    """Defining the rotation matrix using Euler angles"""

    R = np.zeros(shape=(3, 3))
    R[0, 0] = (np.cos(psi)*np.cos(phi)) -
               (np.cos(theta)*np.sin(phi)*np.sin(psi))
    R[0, 1] = (np.cos(psi) * np.sin(phi)) + (np.cos(theta) *
               np.cos(phi) * np.sin(psi))
    R[0, 2] = np.sin(psi)*np.sin(theta)
    R[1, 0] = -(np.sin(psi) * np.cos(phi)) - (np.cos(theta) *
               np.sin(phi) * np.cos(psi))
    R[1, 1] = -(np.sin(psi) * np.sin(phi)) + (np.cos(theta) *
               np.cos(phi) * np.cos(psi))
    R[1, 2] = np.cos(psi) * np.sin(theta)
    R[2, 0] = np.sin(theta)*np.sin(phi)
    R[2, 1] = -np.sin(theta)*np.cos(phi)
    R[2, 2] = np.cos(theta)
    Result = np.dot(R, r)
    return Result
```

```

def fourier(a, k, pos):
    """Use of a fourier series to map spin orientations"""
    a_xy = np.array([a[0], a[1], 0])
    a_z = np.array([0, 0, a[2]])
    fr = a_z*np.cos(np.dot(k, pos)+np.pi) + a_xy*np.sin(np.dot(k,
        pos)+np.pi)
    return fr

def r_mod(r0, r1):
    """Function to determine |r| between the field generating dipole
    and the point being considered"""
    vector = []
    zip_object = zip(r0, r1)
    for r0_i, r1_i in zip_object:
        vector.append(r1_i - r0_i)
    modulus = np.abs(np.sqrt(((vector[0]) ** 2) + ((vector[1]) ** 2)
        + ((vector[2]) ** 2)))
    return modulus

def analytical_sol(moment,r0,r1,abs_r):
    """Analytical solution of the dipole field equation"""
    r = []
    zip_object = zip(r0, r1)
    for r0_i, r1_i in zip_object:
        r.append(r1_i - r0_i)

    r_unit = np.array(r)/abs_r
    m_dot_R = np.dot(moment, r_unit)
    moment = np.array([moment])

    prefactor = 1e-7/(abs_r**3)
    a = (3 * m_dot_R * r_unit)
    b = moment
    B = prefactor*(b-a)
    return B

"""

First the skyrmion lattice full sample space structure is constructed
"""

B_ext = -0.2 # Setting the applied field strength
q_r = 23.5 # Setting the periodicity of the skyrmion lattice
q_mag = 2*np.pi/q_r
x = np.linspace(-100, 100, 201)
y = np.linspace(-100, 100, 201)

```

```

z = np.linspace(-30, 30, 61)

q = [q_mag, 0, 0]
q_init = np.array(q)
a = np.array([0, 1, 1])

# Helices defined using a single q are first applied to the total
# structure

#Q1
A = []
rot1 = -np.pi/3
for k in range(0, len(x)):
    for j in range(0, len(y)):
        for p in range(0, len(z)):
            dir = np.array([x[k], y[j], z[p]])
            pos = [x[k], y[j], z[p]]
            pos = [i * sep for i in pos]
            trans_a = Rot_Mat(rot1+np.pi, 0, 0, a)
            trans_q = Rot_Mat(rot1, 0, 0, q_init)
            direction = fourier(trans_a, trans_q, dir)
            xspin = direction[0].real
            yspin = direction[1].real
            zspin = direction[2].real
            A.append([pos[0], pos[1], pos[2], xspin, yspin, zspin])
#Q2
B = []
rot2 = np.pi
for k in range(0, len(x)):
    for j in range(0, len(y)):
        for p in range(0, len(z)):
            dir = np.array([x[k], y[j], z[p]])
            pos = [x[k], y[j], z[p]]
            pos = [i * sep for i in pos]
            trans_b = Rot_Mat(rot2+np.pi, 0, 0, a)
            trans_q2 = Rot_Mat(rot2, 0, 0, q_init)
            direction = fourier(trans_b, trans_q2, dir)
            xspin = direction[0].real
            yspin = direction[1].real
            zspin = direction[2].real
            B.append([pos[0], pos[1], pos[2], xspin, yspin, zspin])
#Q3
C = []
rot3 = 2*np.pi/6
for k in range(0, len(x)):

```

```

for j in range(0, len(y)):
    for p in range(0, len(z)):
        dir = np.array([x[k], y[j], z[p]])
        pos = [x[k], y[j], z[p]]
        pos = [i * sep for i in pos]

        trans_c = Rot_Mat(rot3+np.pi, 0, 0, a)
        trans_q3 = Rot_Mat(rot3, 0, 0, q_init)
        direction = fourier(trans_c, trans_q3, dir)
        xspin = direction[0].real
        yspin = direction[1].real
        zspin = direction[2].real
        C.append([pos[0], pos[1], pos[2], xspin, yspin, zspin])

#Q4 - due to applied field
D = []
rot4 = 0
qferro = np.array([0,0,0])
b = np.array([0,0,1])
for k in range(0, len(x)):
    for j in range(0, len(y)):
        for p in range(0, len(z)):
            dir = np.array([x[k], y[j], z[p]])
            pos = [x[k], y[j], z[p]]
            pos = [i * sep for i in pos]
            trans_d = Rot_Mat(rot4, 0, 0, b)
            trans_q4 = Rot_Mat(rot4, 0, 0, qferro)
            direction = fourier(trans_c, trans_q3, dir)
            xspin = direction[0].real
            yspin = direction[1].real
            zspin = direction[2].real
            D.append([pos[0], pos[1], pos[2], xspin, yspin, +zspin])
"""

The results of each spiral wave and the ferromagnetic component are
now added together to give the final spin texture
"""

R = []
for i in range(0, len(A)):
    Ar = np.array(A[i][3:])
    Br = np.array(B[i][3:])
    Cr = np.array(C[i][3:])
    Dr = np.array(D[i][3:])
    Total = Ar + Br + Cr + Dr
    mod = np.sqrt((Total[0].real ** 2) + (Total[1].real ** 2) +
                  (Total[2].real ** 2))
    Total = Total.tolist()

```

```

R.append([A[i][0], A[i][1], A[i][2], Total[0] / mod, Total[1] /
mod, Total[2] / mod])

"""
Calculating the magnetic field strength at random positions within a
smaller sample lattice
"""

position = np.array([1.33e-10, 1.98e-10, 1.93e-10])
moments = []

for i in range(0, len(R)):
    s_f = spinmag
    moments.append([R[i][3] * s_f, R[i][4] * s_f, R[i][5] * s_f])

for j in range(0, 30000):
    #Defining the sample lattice space
    x_r = random.randint(-80, 80)*sep
    y_r = random.randint(-80, 80)*sep
    z_r = random.randint(-30, 30)*sep

    location = np.array([x_r, y_r, z_r]) + position
    B_field = []
    for p in range(0, len(R)):
        m_a = np.array(moments[p])
        rs = (r_mod(location, R[p][:3]))
        loc = np.array(R[p][:3])
        [r] = analytical_sol(m_a, location, loc, rs)
        B_field.append(r)

    totalB = [sum(l) for l in zip(*B_field)]
    totalB = totalB + np.array([0, 0, B_ext])
    totalB_mag = (np.sqrt((totalB[0])*np.conj(totalB[0]) +
(totalB[1])*np.conj(totalB[1])) +
(totalB[2])*np.conj(totalB[2])))

    totalB_mag = totalB_mag.real

```

---